Part I
Fluid Dynamics in Microchannels

1
Multiphase Flow*

Axel Günther and Michiel T. Kreutzer

1.1
Introduction

We start our discussion by emphasizing how flow behavior is related to the transport of molecules and chemical reactions in micrometer- and submicrometer-sized channel networks. We discuss measurement of flow and transport properties and demonstrate how these characteristics translate to a range of different microfluidic applications: multiphase flow through porous media [1], human airways [2], miniature cell-biological systems [3, 4], flow in microfluidic catalytic monoliths [5] and the use of interfacial forces as a means for actuation in microdevices [6]. The discussion of multiphase microfluidic systems in this chapter complements several recent reviews on general aspects of transport phenomena in microfluidic systems [37, 174–179].

Multiphase flows provide several mechanisms for enhancing and extending the performance of single-phase microfluidic systems. The long diffusion times and broad dispersion bands associated with single-phase pressure-driven flow can be reduced by adding a second, immiscible, fluid stream. Multiphase flows form when two or more partially or not miscible fluids are brought in contact and subjected to a pressure gradient. The resulting flows display a rich phase behavior, e.g. as suspended droplets, bubbles, slugs or thin films. The flow behavior is dependent on the relative flow rates of the fluid phases involved, the resulting interaction between gravitational, interfacial, inertial and viscous forces and the wetting behavior of the channel walls. The alternating succession of immiscible fluid segments will play a particularly important role. We refer to this flow condition as segmented flow and will associate with it a number of favorable conditions, including enhanced mixing, increased mass transfer across phase boundaries and reduced dispersion. These effects enhance reaction yields and mixing. Multiphase microchemical systems generally take advantage of the large interfacial areas, rapid mixing and reduced mass

*A List of Symbols and Abbreviations can be found at the end of this chapter.

Micro Process Engineering, Vol.1: Fundamentals, Operations and Catalysts
Edited by V. Hessel, A. Renken, J.C. Schouten, and J.-I. Yoshida

ISBN: 978-3-527-31550-5

transfer limitations [7, 8] to achieve improved performance relative to conventional bench-scale systems [9–11]. Examples of gas–liquid reactions that were performed in microreactors include direct fluorination [12–20], chlorination, bromination, sulfonation and oxidation reactions. Microreactors have further been suggested to advance the sustainability of organic synthesis [21]. Another category concerns heterogeneous catalytic reactions, involving gas–liquid–solid or liquid–liquid–solid systems such as hydrogenation [22–25]. In the case of liquid-phase reactions, a second immiscible fluid is introduced solely to improve the transport properties in the continuous liquid phase, i.e. to enhance mixing and reduce the unwanted effect of axial dispersion. The use of isolated, well-mixed droplets permits kinetic studies of organic reactions at the millisecond time scale along with characterization of synthetic reaction networks [26]. Similarly, segmented flows of liquid slugs that are separated by gas bubbles improve synthesis and overcoating of nanoparticles with narrow size distributions [27–31]. Liquid droplets also allow the isolation and concentration of protein solutions in crystallization studies [32, 33]. Blood analysis in segmented flow in capillaries represents an early example of multiphase microfluidics [34]. Recent biological applications include DNA analysis [35], cell encapsulation [36] and cell stimulus and lysis [4].

We begin in Section 1.2 by considering the forces and time scales governing multiphase flows in 10 nm–500 μm wide microchannels. In addition to interfacial forces acting on fluid–fluid interfaces and on microchannel walls, multiphase microfluidic networks are affected by gravitational, inertial and viscous forces. Interplay of these forces gives rise to flow instabilities, rich dynamics and a variety of possible fluid phase distributions, that are described in Section 1.3. Section 1.3 also introduces passive, surface tension-driven means for separating two fluid phases in microfluidic systems. The influence of channel geometries on flow behavior is discussed in Section 1.4. Section 1.5 introduces practical aspects associated with scaled-out multiphase microreactors. Different numerical and experimental techniques are available to probe multiphase flows, related transient flow behavior, phase distributions, mixing and dispersion characteristics. Section 1.5 compares these methods based on their spatial and temporal resolution, and also the potential for integration into scalable systems where convenient flow observation in multiple microfluidic channels is required. In Section 1.6, we discuss steady flows. In Section 1.7, we focus on droplet- and bubble-based systems. Characteristics of microscale gas–liquid and liquid–liquid flows are discussed separately. Finally, we discuss several practical aspects relating to integrated networks of multiphase systems in Section 1.8.

1.2 Fundamentals of Multiphase Flow

In this section, we first introduce interfacial tension and consider a resting fluid interface, and discuss its interaction with a microchannel wall. We continue with consideration of dynamically moving fluid interfaces that are relevant to multiphase microflows. The different body forces, gravitational, viscous and inertial effects are

compared to interfacial forces. In most cases, we find that interfacial forces dominate by several orders of magnitude.

1.2.1 Properties of Fluids and Interfaces

Under steady flow conditions and with negligible gravitational acceleration g and temperature gradients, two fluid phases are in equilibrium if the pressures in both phases are uniform and differ from each other only in the capillary pressure that is given by the Young–Laplace equation, $\Delta P_{cap} = \gamma\kappa$, where γ is the interfacial tension and κ is the local mean curvature at the interface [6, 37]. We will use γ in general and γ_{12} to specifically denote the interfacial tension between the fluids 1 and 2. Symbol $\sigma = \gamma_{1g}$ denotes the surface tension, the interfacial tension between a liquid and a gas phase. Depending on the interface curvature (Figure 1.1a), interfacial forces either

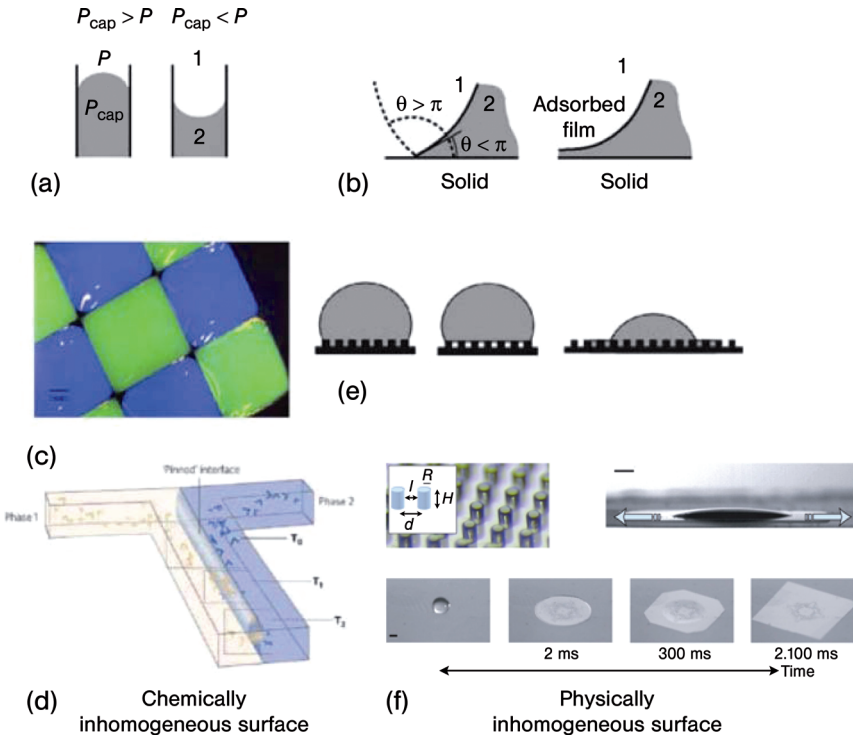

Figure 1.1 (a) Positive and negative differences between the capillary pressure, P_{cap}, and the ambient pressure, P, that result from an either positive or negative curvature of an air–liquid interface [42]. (b) Local configuration in the three-phase region. Left, the two fluid phases (1 and 2) and the solid wall intersect at a contact line with angle h; right, the fluid phases are separated by an adsorbed film [37]. Pinning fluid–fluid interfaces by chemically inhomogeneous surfaces in static (c) [180] and flowing systems (d) [43]. Altering the wetting properties using chemically homogeneous, micro- and nanostructured surfaces: (e) [38–40], (f) [44].

reduce or increase the pressure P_{cap} in the liquid in comparison with the ambient pressure, P. For example, the capillary pressure at a water–air interface in a 100 μm wide hydrophilic microchannel is approximately 1.5 kPa and it becomes very large at submicrometer scales, approximately 1.5 MPa for a 100 nm wide channel.

1.2.1.1 Microchannel Surface Characteristics and Wetting

Solid surfaces are characterized by their roughness and wetting behavior, which is determined by the contact angle. The gas–liquid–solid contact angle θ is shown in Figure 1.1b. When a static fluid interface appears to touch a wall, two local configurations can be distinguished by enlarging the three-phase region (Figure 1.1b). The fluid interface either touches the wall and forms a contact line between the three phases, or an adsorbed film separates the second fluid from the wall [6, 37]. The first case is described by the contact angle θ, which is related to the interfacial energies of the solid, s, and two fluid phases 1 and 2 by Young's equation, $\gamma_{12}\cos\theta = \gamma_{1s} - \gamma_{2s}$. Wetting liquids have small contact angles approaching zero and non-wetting liquids have large contact angles going towards 180°. Ajaev and Homsy ([37] and references therein) provide a detailed discussion including the case of an adsorbed film. Figure 1.1c and d give examples of hydrophobic– hydrophilic patterned surfaces in static and flowing systems. For micropatterned surfaces, the two properties are interrelated since the contact angle is a macroscopic quantity. Wetting properties can therefore be altered either by chemically modifying surface properties (Figure 1.1c and d) or by introducing a micro- or nanoscale surface roughness elements (Figure 1.1e and f), i.e. altering the microchannel roughness can result in different contact angles even if the same surface treatment is used. Figure 1.1(e) demonstrates how contact angles for hydrophobic, micropatterned surfaces vary depending on the pattern density and radius of curvature and generate macroscopically super-hydrophobic surfaces [38–40]. Micrometer- or submicrometer-scale roughness elements are routinely introduced during the microfabrication process and are sometimes even purposefully included. Side-wall roughness is often caused either by the limited resolution of a lithography mask or from the subsequent dry etch and passivation cycles during deep reactive ion etching (DRIE). During DRIE, roughness elements at the bottom wall can also build up, depending on the etching recipe used. Silicon wet etching in KOH solution offers atomically smooth surfaces. Replica molding of PDMS allows the reliable transfer of patterns from a microfabricated master at submicron resolution. Variations in surface tension induced by chemically patterned surfaces [6, 41] were used for thermocapillary droplet actuation.

Various fabrication techniques have been developed to alter wetting behavior of microfabricated surfaces either permanently or temporarily. In addition to the pressure-driven flow through microfluidic channels considered here, "channel-free" methods for manipulating droplets (of generally larger size) on electrode arrays below a hydrophobic layer have been introduced [45–48]. These electrowetting-on-dielectric (EWOD) systems depend critically on the ability to deposit hydrophobic and electrically isolating coatings consistently on top of the electrode arrays. Popular choices are spin-coated fluoropolymers (e.g. Cytop, Asahi Chemicals) [47], parylene

and polydimethylsiloxane. In addition to transporting droplets, changing the wetting characteristics by EWOD can also be used to induce mixing, as demonstrated by Nichols and Gardeniers and, who combined droplet transport, merging, splitting and mixing using EWOD to determine fast kinetics [49].

1.2.1.2 Scaling of Forces

In flowing systems, the complex interplay between interfacial, gravitational, viscous and inertial forces is responsible for a variety of phase distributions and flow patterns. The dominant interfacial forces combined with the laminar nature of the flow result in very regularly shaped gas–liquid and liquid–liquid interfaces characteristic of multiphase microflows. Courbin *et al*. described dynamic wetting morphologies of a flat surface that is microstructured with a forest of posts upon droplet impact [44]. Eijkel and co-workers [42, 48] provided a more general review of surface tension effects in the context of nanofluidic systems. The importance of interfacial forces with respect to gravity is described by the dimensionless Bond number, $Bo = (\Delta\rho)g d_h^2 \sigma^{-1}$, where $\Delta\rho$ is the density difference between the two immiscible fluids (gas–liquid, liquid–liquid) and d_h the characteristic channel dimension, the hydraulic diameter ($d_h = 4A/\Gamma$, where A is the channel cross-sectional area and Γ is the wetted perimeter).

Ranking the importance of different forces helps in categorizing the increasing number of experimental studies with the ultimate goal to predict multiphase flow behavior in microchannel networks and formulate guidelines for their design. Multiphase microflows are characterized by the ratio of viscous to surface forces, the capillary number (Ca) and by the ratio of fluid viscosities:

$$Ca = \frac{\mu U_d}{\sigma}\frac{\mu}{\mu_d} \tag{1.1}$$

where μ and μ_d are the viscosities of the continuous and the dispersed phases, respectively. The ratio of inertia to surface forces is expressed by the Weber number:

$$We = \frac{\rho U_d^2 d_h}{\sigma} \tag{1.2}$$

As for single-phase flows, the Reynolds number, $Re = We/Ca$, relates viscous and inertial forces and is fixed for given We and Ca. Figure 1.2 [50] shows how Bond, capillary and Weber numbers, i.e. the relevant forces with respect to the interfacial force, vary if the channel hydraulic diameter, d_h, and the velocity, U_d, are altered. The thickness of the planes obtained represents the practical range of fluid properties for organic–gaseous, organic–aqueous and aqueous–gaseous systems. The conditions at which interfacial forces dominate over gravity, inertial and viscous forces corresponds to low velocities and small microchannel sizes. Only if U_d is on the order of several meters per second or in the presence of very large accelerations of liquids, e.g. at the initial stage of rapid expansion of a vapor bubble, does inertia dominate over gravity and viscous forces [37, 51, 52]. Under such conditions, bubbles and drops much

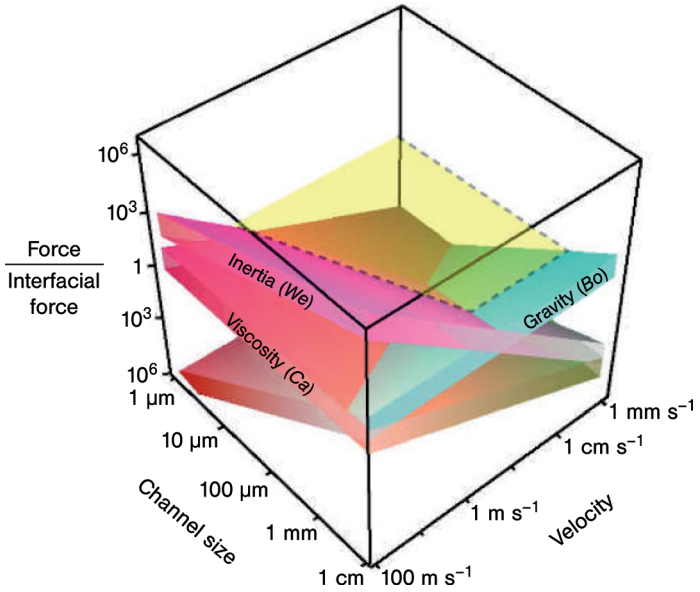

Figure 1.2 Inertial, viscous and gravitational body forces, relative to interfacial forces, as a function of the channel size and characteristic velocity in microfluidic multiphase systems [50].

smaller than d_h can be formed, and microscale gas bubbles can be entrained, potentially resulting in fluid interfaces with complex shapes or interfacial instabilities.

1.2.1.3 Surface Tension Variations

Surface tension variations affect the mobility of the fluid–fluid interface and cause Marangoni flow instabilities. Surfactant-laden flows exhibit surface tension variations at the gas–liquid or liquid–liquid contact line due to surfactant accumulation close to stagnation points [2, 53]. For gas–liquid systems, these Marangoni effects can often be accounted for by assuming "hardening" of the gas bubble, i.e. by replacing the no-shear boundary condition that is normally associated with a gas–liquid (free) boundary with a no-slip boundary condition. It should be noted that such effects can drastically alter pressure drop in microfluidic networks and theoretical predictions based on no-shear at free interfaces must be used with care in practical applications [54].

1.2.1.4 Particles and Fluid Interfaces

Particles with characteristic dimensions (e.g. particle diameters) between a few nanometers (e.g. metal and semiconductor nanoparticles, quantum dots and rods) and several micrometers (polymere microspheres, catalyst particles, biological cells) play an important role in a variety of microfluidic systems. Depending on the available residence time, their size d_p and the density ratio between the particle and fluid phases, ρ_P/ρ, particles will settle within the microchannel or can be transported through it without sedimentation. In most applications (flow of suspended cells,

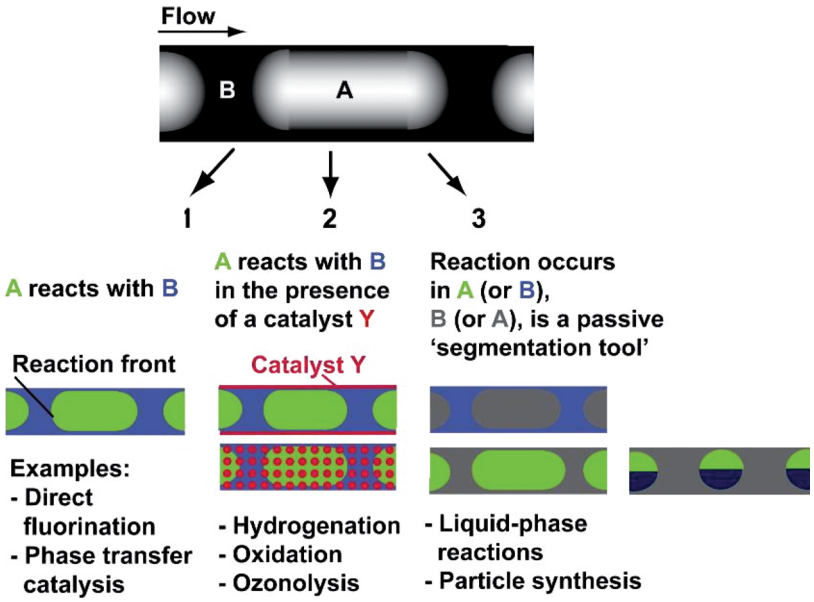

Figure 1.3 Multiphase systems for performing reactions in microscale segmented flow. The continuous phase (A) is shown in green and the disperse phase (B) is colored blue. (1) Immiscible fluids, either a gas–liquid mixture or two liquids, react with each other. The location of the reaction depends on the reaction rate, as infinitesimally fast reactions form a front at the fluid interface [12–18, 55]. (2) Immiscible fluids react with each other in the presence of a catalyst. (3) The reaction occurs solely in one phase (either continuous or dispersed); the second phase provides a passive 'tool' for flow segmentation [27–30].

solutionphase particle synthesis), sedimentation and the resulting accumulation of particles within a microchannel are unwanted.

1.2.2 Classification of Phase Distributions

Figure 1.3 shows a representative distribution between a continuous and an immiscible dispersed phase that we refer to a *segmented flow*. Segmented flows exist both in gas–liquid mixtures and in immiscible liquids. They can be produced with great regularity in microfluidic devices. The resulting phase distributions are sometimes also referred to as "digital" microflows or "digital microfluidics" – terms that are used in a somewhat different context for electrically driven droplets.

1.3 Dynamic Behavior of Multiphase Microflows

In Section 1.2 we have discussed the important role of surface tension in multiphase flows through microchannel networks. This behavior is in stark contrast to

single-phase microflows. We discuss in this section the mechanisms that cause a rich variety of different fluid phase distributions to be formed. The different phase distributions or flow regimes and the conditions for their formation are summarized for microscale gas–liquid and liquid–liquid flows. At the end of the section, we discuss different microscale solutions for the complete separation of multiphase flows into single-phase streams.

1.3.1 Flow Instabilities

When immiscible fluid streams are contacted at the inlet section of a microchannel network, the ultimate flow regime depends on the geometry of the microchannel, the flow rates and instabilities that occur at the fluid–fluid interface. In microfluidic systems, flow instabilities provide a passive means for co-flowing fluid streams to increase the interfacial area between them and form, e.g. by an unstable fluid interface that disintegrates into droplets or bubbles. Because of the low Reynolds numbers involved, viscous instabilities are very important. At very high flow rates, however, inertial forces become influential as well. In the following, we discuss different instabilities that either lead to drop/bubble breakup or at least deform an initially flat fluid–fluid interface. Many important phenomena relate to classical work on the stability of unbounded viscous flows (see e.g. the textbooks by Drazin and Reid [56] and Chandrasekhar [57]). We will see, however, that flow confinement provides a number of new effects that are not yet fully understood and remain active research topics.

1.3.1.1 Capillary Instability

The formation of droplets or bubbles in microfluidic devices relates to the classical treatment of a capillary instability at a sheared, cylindrical interface in an unbounded flow was described by Plateau and Lord Rayleigh [58, 59]. In microfluidic devices, such instabilities allow the formation of monodisperse bubbles or drops in the flow focusing configuration shown in Figure 1.4a. Ganan-Calvo's group was the first to form microbubbles at relatively high Reynolds numbers, *Re*, between 10^2 and 10^3 [60, 61]. For the flow-focusing experiments in microfluidic devices that were pioneered by the groups of Stone, Whitesides and Weitz [62, 63], *Re* is much smaller, typically between 0.01 and 1, interfacial forces dominate and the influence of inertia is often small compared with viscous effects. In difference to the classical treatment of unbounded flows, fluid confinement between microchannel walls affects the breakup of a cylindrical liquid or gas core into droplets or bubbles [64, 65]. In many applications, a capillary instability is expected to produce liquid–liquid [62, 63, 66] or gas–liquid [67, 68] segmented flows with uniform droplet or bubble sizes. Several attempts have focused on characterizing the rich dynamic behavior of segmented microflows that also includes very irregular flow behavior. Kraus *et al.* [69] measured statistical properties (distribution of liquid slug and gas bubble lengths) in segmented gas–liquid flow and documented the sensitivity to external disturbances (e.g. syringe pump pressure fluctuations). Garstecki *et al.* [65, 70] probed the dynamics of a single-channel microfluidic bubble generator by analyzing the phase distribution

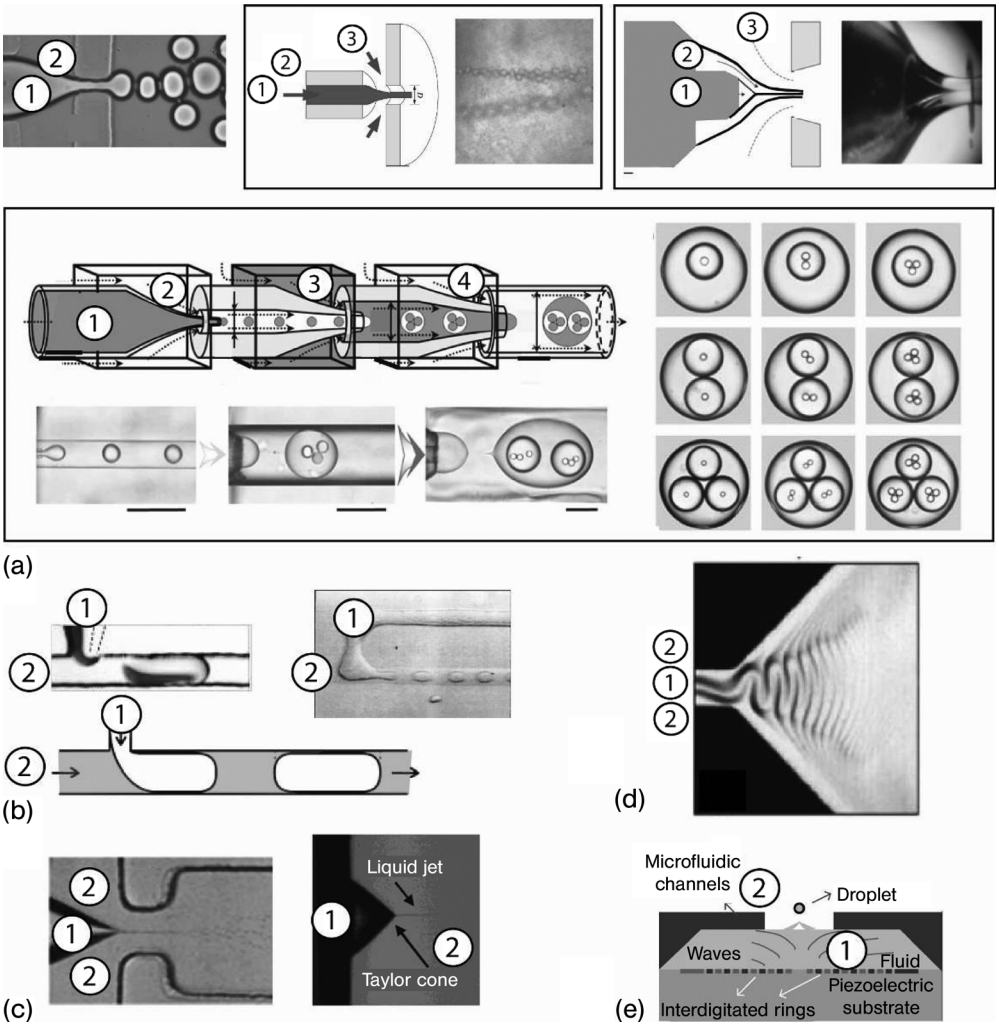

Figure 1.4 Flow instabilities relevant to multifluid systems in microchannel networks. The different miscible or immiscible phases are indicated as 1, 2, 3 and 4. (a) Breakup in a flow-focusing geometry [62, 181] due to a Rayleigh–Plateau instability. Bubble and droplet chains and multiple emulsions were prepared [71]. (b) Pressure-induced breakup [64, 72, 182]. (c) Taylor cone formation in a flow-focusing configuration with a ratio of 350:7 of outer to inner flow rates and an applied voltage of 2000 V [73, 74]. (d) Formation of liquid threads using miscible liquid streams with different viscosities [75, 76]. (e) High-rate droplet production during acoustic streaming [77]. Cases (a–c and e) are concerned with immiscible fluids; case (d) considers two miscible fluid streams.

that was determined from ensembles of micrographs and suggested such flows as a model system for studying complex systems in space and time. Pressure drop - induced breakup. At low capillary numbers, Garstecki *et al.* [64] demonstrated that breakup of drops or bubbles at a microfluidic T-junction (Figure 1.4b) does not occur

due to shear stress but due to the pressure drop across the emerging bubble or drop. As a function of increasing *Ca*, three different regimes for the formation of droplets and bubbles can be identified: squeezing, dripping and jetting [64]. Garstecki *et al.* demonstrated that droplet/bubble formation in the squeezing regime is induced by pressure fluctuations during breakup and is independent of *Ca*.

1.3.1.2 Deformation of Stratified Liquid Layers

The Kelvin–Helmholtz (KH) instability causes the sheared interface between two fluids that move horizontally at different velocities to form waves (Figure 1.4d). Below a threshold value, surface tension stabilizes the interface. Above the threshold, waves of small wavelength become unstable and finally lead to the formation of drops (liquid–liquid flows) or bubbles (gas–liquid flows), defined by the microchannel dimensions. Surface tension will suppress the KH instability if [57]

$$(U_1 - U_2)^2 < 2\sqrt{g\sigma(\rho_1 - \rho_2)}\,\frac{\rho_1 + \rho_2}{\rho_1 \rho_2} \tag{1.3}$$

where ρ_1, ρ_2 and U_1, U_2 are the densities and velocities of the phases 1 and 2, respectively. Relative velocities of several meters per second are needed to destabilize gas–liquid systems; velocities that are considered very large in most microfluidic applications. However, for liquid–liquid flows with fluids of similar density, e.g. ethanol ($\rho_1 = 790\,\mathrm{kg\,m^{-3}}$) and paraffin oil ($\rho_2 = 830\,\mathrm{kg\,m^{-3}}$), the required velocity difference can be as low as $0.1\,\mathrm{m\,s^{-1}}$ – conditions relevant to microfluidics. Funada and Joseph [78] discussed the particular case of viscous KH instability in a rectangular channel.

1.3.2 Multiphase Flow Regimes

Many flow patterns have been obtained for two-phase flow in capillaries of circular cross-section (Figure 1.5a). Although quantitative methods, e.g. void fraction measurements, are under development, the description of flow patterns is often based on a qualitative and sometimes somewhat subjective visual discrimination. Most researchers present "representative" pictures along with the observed flow pattern map for clarity.

With the aforementioned limitations in mind the number of different flow patterns may be reduced to the following four:

1. *Bubbly flow.* When the flow rate of the non-wetting phase is much lower than the one of the wetting phase, droplets/bubbles with diameters that are smaller than the microchannel size are formed it. If stabilized by surfactants, these droplets or bubbles are stable for extended periods of time without coalescence, especially when the volume fraction of the disperse phase is small.

2. *Segmented flow.* When the ratio of flow rates for the wetting to the non-wetting phases is close to unity, the dispersed phase forms droplets or bubbles that span most of the cross-section of the channel. Two consecutive droplets confine the continuous liquid phase between them.

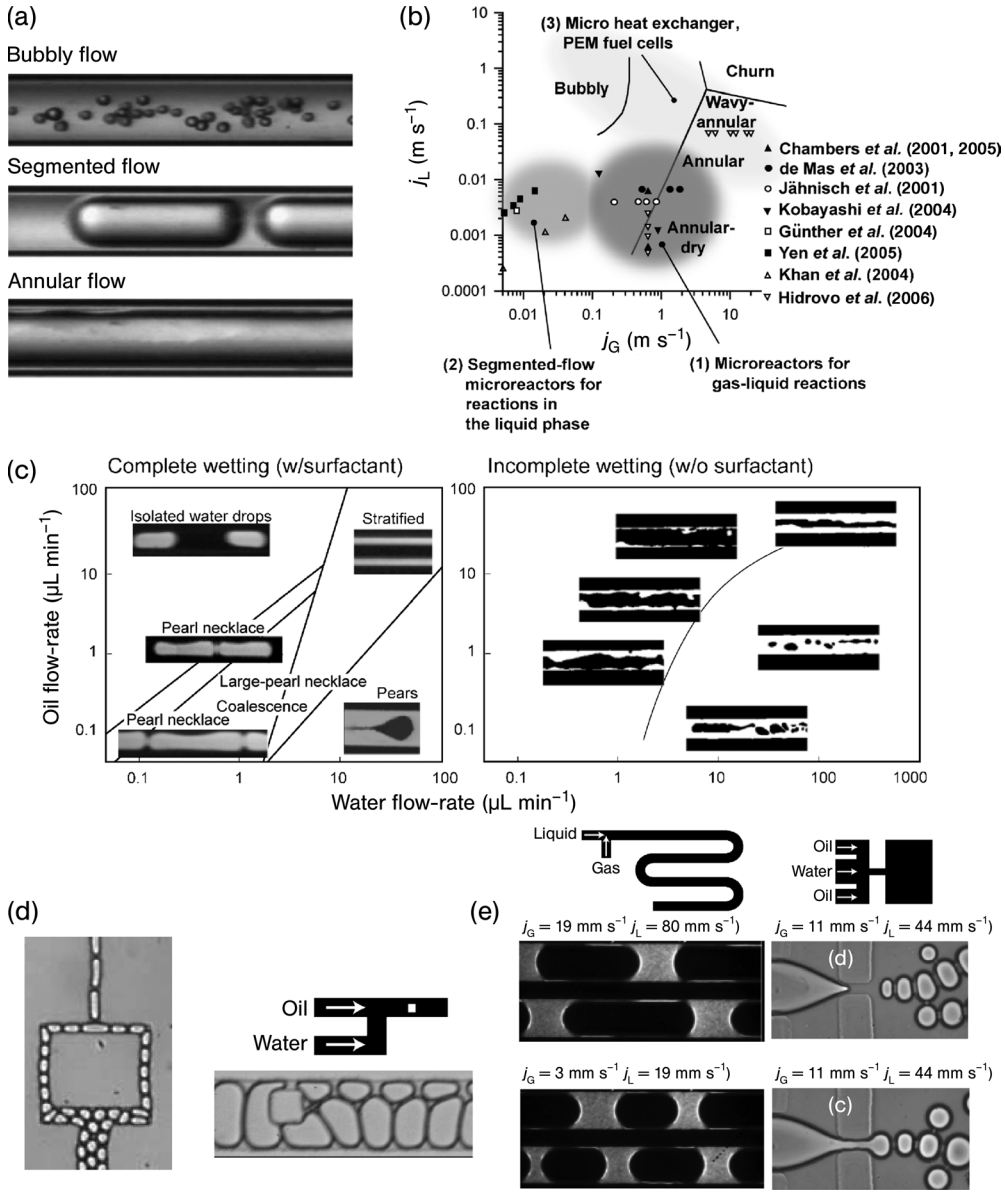

Figure 1.5 Flow patterns. (a) The most common flow patterns are bubbly flow, segmented flow and annular flow [79]. (b) A flow map, indicating the ranges of gas and liquid velocity for which the various flow patterns are observed in a given device [80]. These flow maps have to be used with care, as the pattern is not determined by velocities alone, such as wettability, channel geometry and inlet geometry (c–e). (c) Impact of wetting on observed flow patterns for a liquid–liquid flow [81]. (d) Transition from a segmented flow in which the dispersed phase spans the entire cross-section to a bubbly flow [63]. (e) T-junctions result in segmented flow for a wide range of flow conditions [64], as shown here with micrographs taken under conditions similar to those in a flow focusing device [62] that uses a small orifice to create bubbly flows of small droplets or bubbles over a wide range of conditions.

3. *Annular flow.* When the ratio of flow rates for the wetting phase to the non-wetting phase is very small, the wetting phase is confined to the wall, flowing as an annular film. In channels with non-circular cross-section the film thickness varies considerably along the perimeter, with a significant liquid volume confined to the microchannel corners. The film may become wavy as a result of the interaction with the non-wetting phase at higher velocities.

4. *Churn flow.* At very high velocities, regular flow patterns cease to exist and a chaotic flow appears, in which the sizes and shapes of droplets/bubbles vary widely.

Depending on the wetting properties of the microchannel walls, the lubricating films of the continuous phase, that are found in segmented and annular flow, may break into droplets of a characteristic size $\sim d_h$.

Flow maps can be constructed by arranging the experimentally observed phase distributions inside a microchannel in a diagram with the liquid superficial velocity on the ordinate and the gas superficial velocity on the abscissa (Figure 1.5b and c). The superficial velocity is defined as the volumetric flow rate of the respective phase divided by the cross-sectional area of the microchannel. The experimentally determined flow patterns are often identified with different symbols in the diagram and lines are used to indicate flow regime transitions. Flow regime diagrams may give the impression that the flow rates are the main parameters involved in predicting which flow pattern occurs. This is not the case, as can readily be seen by comparing maps from different references. Which flow pattern actually occurs in a given microchannel also depends on the fluid properties, the wetting behavior of the channel surface, the channel diameter, its cross-sectional shape and the entrance conditions. Even when dimensional analysis is used to reduce the number of parameters, the number of dimensionless groups remains large and most flow maps in the literature are applicable only close to the conditions under which they were obtained. Systematically characterizing multiphase microflows over significant ranges of parameters and meaningful dimensionless representation of the results obtained will be important in arriving at a more general understanding of flow regime behavior.

Droplets and bubbles in microchannels are very stable, in particular when surfactants are added. As a result, one should focus on the conditions at the inlet of the channel. Once formed, droplets and bubbles of a given size often remain intact when carefully expanded within a microchannel network. As is shown in Figure 1.5, a two-phase stream that was generated as a segmented flow may well become a bubbly or foam-like flow.

Quasi-stable droplets and bubbles in microchannels can, when given enough time, undergo flow pattern transitions due to either coalescence or slowly growing disturbances. The amplitude of the disturbances introduced at the inlet can have a profound effect on flow patterns. Galbiati and Andreini [82] demonstrated that a smooth introduction of gas and liquid into the capillary channel resulted in stratified and dispersed flow. By introducing only a single miniature wire into the water feed line of the channel, these flow patterns vanished completely and only slug flow and

annular flow were observed instead. A similar effect was observed by using a very long calming section that allowed small disturbances to grow.

Although most flow maps are presented without attempting to account for the effect of fluid properties and channel diameter, some noticeable exceptions exist. Rezkallah's group [83, 84] obtained flow maps for liquid–liquid systems and discussed the differences from gas–liquid systems. Suo [85] performed experiments using octane, heptane and water as liquids and helium, nitrogen and argon as gases. No significant changes were found for the different gases and the groups ρ_G/ρ_L and μ_G/μ_L were eliminated from consideration. The transition from slug to churn flow was suggested as $ReWe = 2.8 \times 10^5$.

1.3.3
Formation of Multiphase Flow

In many applications, a capillary instability is expected to produce liquid–liquid [62, 63, 66] or gas–liquid [67, 68] segmented flows with uniform droplet or bubble sizes. Several attempts have focused on characterizing the rich dynamic behavior of segmented microflows that also includes very irregular flow behavior. The most common geometry to generate such a stream of segments is a simple T-junction in which the disperse phase is injected from a side channel into the main flow channel. Garstecki *et al.* [64] (see Section 1.3.1.1) demonstrated that droplet/bubble formation in the squeezing regime can be described using a simple balance equation. In this regime, the length of the droplet (or bubble) scales as

$$\frac{L_d}{W_d} \sim 1 + \frac{Q_d}{Q_c} \tag{1.4}$$

where Q_c and Q_d are the flow rates of the dispersed phase and the continuous phase, respectively, and W_d is the width of the disperse-phase inlet channel. The proportionality constants for this scaling relation depend on several aspect ratios of the T-junction, but hardly vary with fluid properties. Because $Ca \ll 1$, the interface of the forming bubble maintains the shape that minimizes the surface area, independent of Ca. Geometry plays an important role, especially in non-round channels: van Steijn *et al.* [86] demonstrated that significant leakage occurs past the forming droplet in the gutters, which reduces the speed with which the interface is squeezed, leading to longer droplets or bubbles in channels of near-square cross-section.

1.3.4
Susceptibility of Multiphase Flow to Pressure Fluctuations

In multiphase microfluidics, transient phenomena can be divided into fluctuations that are flow induced (inside the channel) and induced by external fluctuations. Kraus *et al.* [69] measured statistical properties (distribution of liquid slug and gas bubble lengths) in segmented gas–liquid flow and documented the sensitivity to external disturbances (e.g. syringe pump pressure fluctuations). Van Steijn *et al.* [87] investigated such fluctuations in detail for low-velocity flow in a short

channel. Under these conditions, the pressure jump associated with the release of a droplet from the channel causes a significant pressure pulse that dominates all other contributions.

External fluctuations that are induced by syringe pumps [69, 88] often translate into time-dependent flow rates and potentially even changes in the flow regime. The origin of such fluctuations during steady mechanical driving, as opposed to steady upstream pressure, is related to fluid elasticity and is known as the "bottleneck" effect [89, 90]. The start-up times that are caused by this effect can be surprisingly long, even for liquid flow. Another contribution to long transients can come from the flexibility of feed tubing [90]. Reinecke and Mewes [91] considered a compressible gas section directly upstream of a segmented flow channel, which leads to fluctuations that are proportional to the volume of that channel. Such fluctuations, which can take a very long time to vanish during start-up, can be reduced by placing a high hydrodynamic resistance in the gas feed directly upstream of bubble-generating sections such as the above-mentioned T-junctions. De Mas *et al.* [18] created a horizontally and vertically scaled-out microfluidic reactor with 60 parallel channels that are each fed with gas and liquid through such a high hydrodynamic resistance, in order to achieve a steady distribution of both phases (see also section 1.8).

1.3.5 Separation of Phases

Phase separation in macroscale equipment either uses density differences between the two fluids to drive the separation, as in settlers, or these differences play an important role in the technical layout of the separator, e.g. in distillation towers. In macroscopic two-phase flow, length scales vary between the size of the apparatus and the interface-dictated Laplace length scale ($\sqrt{\sigma/(g \cdot \Delta\varrho)}$) of entrained bubbles or drops. The former is often on the order of meters, whereas the latter is on the order of millimeters. This significant disparity in length scales makes it virtually impossible to separate macroscopic two-phase flows in a single step.

In microfluidic systems, however, gravitational body forces and associated density differences are small and most separations are based on surface forces rather than body forces. The equipment length scales shrink to values smaller than the Laplace scale. Complete separation of multiphase microflows therefore becomes possible in a single step. Günther *et al.* [92] fabricated a gas–liquid separator as a capillary-based system that separates mixtures of gases and wetting liquids, independent of flow regime and at liquid flow rates varying over three orders of magnitude, between $\sim 1\,\mu l\,min^{-1}$ and $2\,ml\,min^{-1}$ [50]. By wetting the capillaries, the liquid phase prevented the gas from penetrating into the capillary matrix as long as the applied pressure was less than the breaking pressure that is equivalent to the capillary pressure, $p_{cap} = 3$–$10\,kPa$. The applied pressure forced the liquid through the capillaries separating the gas–liquid mixture. The capacity of the separator depended on the size and number of capillaries. For typical synthesis conditions, the upper demonstrated limit of $2\,ml\,min^{-1}$ corresponds to amounts typically produced in 200–1000 parallel multiphase reaction channels. Hibara *et al.* [93] demonstrated the

separation of bubbly gas–liquid flows in a hydrophilic–hydrophobic patterned microchannel network that was fabricated using a two-step photolithographic wet-etching technique and had a breaking pressure of 1.1–7.7 kPa. The breaking pressure determines the operating limit of the separator and hence the robustness of the system to pressure fluctuations. Kralj *et al.* [94] extendet the gas-liquid seperator design to liquid–liquid separations, using a membrane with a narrow pore size distribution in place of a row of slits. For liquid–liquid separations, viscous pressure losses are larger and interfacial tensions are generally lower, which requires smaller feature sizes in order to obtain practical windows of operation. Instead of microfabricating these features, Kralj *et al.* integrated a porous hydrophobic membrane into the device.

1.4 Role of Channel Geometries

The previous section provided an overview of instabilities that lead to a rich variety of different multiphase flow regimes that can be obtained in microchannel networks. Two-phase flow in well-defined geometries has been investigated in great detail. A closer look reveals that many of the underlying theories were originally developed either for an unbounded system (no channel walls) or for channels of circular cross-section. Computational and theoretical studies favor round channels in which only two-dimensional, i.e. axisymmetric, solutions are required. In contrast, for many microfluidic channel networks the layout of the microchannel network is lithographically defined in a 2D plane and then "extruded" into the third dimension, either by etching the bulk material (e.g. dry etching in silicon, glass and quartz) or by patterning the channel into a layer of negative resist (e.g. SU-8), resulting in (near) rectangular cross-section microchannels with close to vertical side-wall profiles. Dry etching tools are standard equipment in most university-based or commercial microfabrication foundries for microelectromechanical systems (MEMS).

Abrasive jet machining (AJM) [95, 96] and excimer laser-based ablation tools, which require micromachined masks, are starting to become commercially available and provide relatively high writing speeds. The resulting microchannels can have very large aspect ratios and are characterized by slanted side-walls. The deposition of debris at the surfaces close to the machined channel features can be a point of concern for microfluidic devices during subsequent bonding. Femtosecond laser writing is very time consuming for microchannels that are relatively large (>100 μm wide and deep) but provides excellent smoothness of surfaces.

Channels that are patterned by isotropic etching have rounded corners in the cross-section and channels that are patterned by KOH etching have a triangular or trapezoidal shape.

Extrapolating theoretical predictions for axisymmetric studies to non-round channels must be done with considerable care for multiphase microfluidics. For bubbly flows the impact of channel shape is less important. In contrast, for droplet

systems where the dispersed phase has dimensions comparable to the channel size, the effect is considerable. The dominance of surface tension ensures that fluid– fluid interfaces maintain smooth curvatures and conform poorly to the sharp microchannel corners. Figure 1.6a shows the influence of the microchannel cross-section on microscale segmented flow for different capillary numbers. For the non-uniform lubricating films and long droplets and bubbles, Wong *et al.* made theoretical predictions for various polygonal channel shapes (Figure 1.6b) [97, 98]. A numerical study was conducted by Hazel and Heil [99, 100]. Experimental confirmation of such

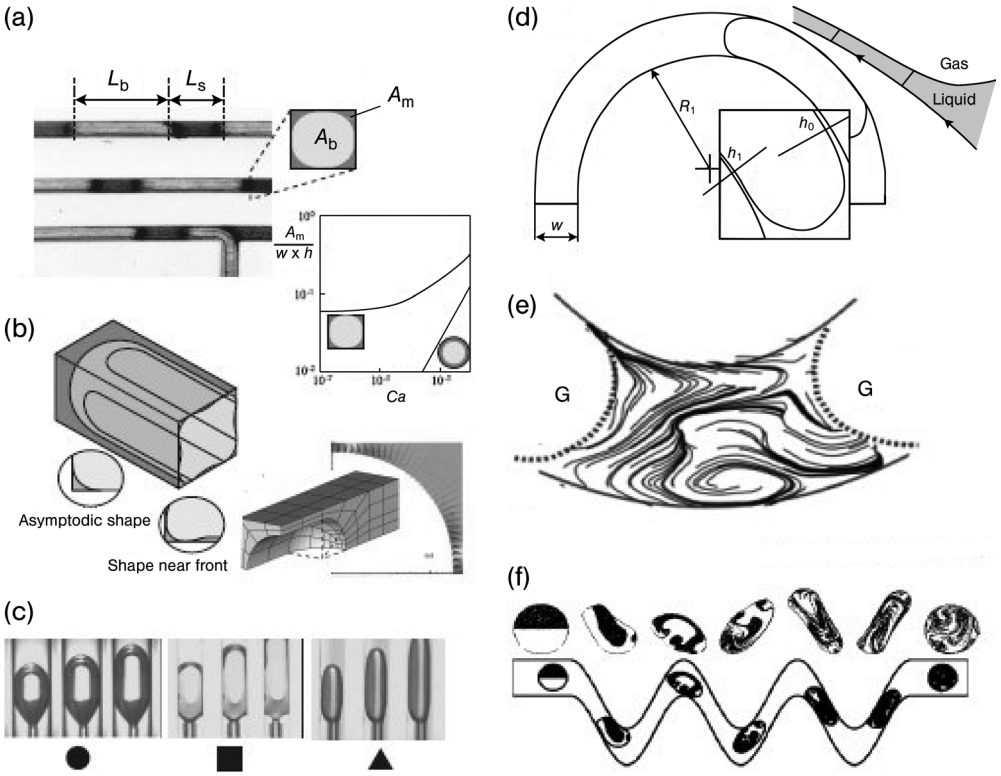

Figure 1.6 Geometry of ducts, impact of cross-sectional shape (a–c) and impact of bends (d–f). (a) Relevant geometries in segmented flows, including the shape of the menisci between the channel wall and dispersed phase. The graph shows what fraction of the cross-sectional area the menisci fill for round and square channels, as a function of *Ca* [104]. (b) Evolution of meniscus shape in square channels [97]. The shape at the front of the bubble is markedly different from that at the tailing end. The numerical grid and computed film shape and velocity field were obtained using a flexible-mesh finite element analysis [99]. (d) In serpentine channels, the inner film meniscus is thinner than the outer meniscus, which can be analyzed using a curvature-corrected lubrication analysis [105]. (e) This difference in leakage breaks the symmetry of the flow in the segments of the continuous phase, enhancing mixing across the centerline [106]. (f) A similar effect of mixing enhancement, resulting in the chaotic baker's transformation mixing, is observed for the dispersed phase [107].

predictions is limited (e.g. [101–103]), especially for the low flow rates ($Ca < 0.01$) that are predominant in microfluidic applications.

Apart from the microchannel cross-section, the impact of non-straight channels is crucial, especially for mixing applications, where serpentine channels have been shown to break symmetry and enhance mixing in bubbles [106]. Note that this enhanced mixing is due to chaotic advection in Stokes flow. Dean vortices, i.e. secondary flow patterns due to centrifugal inertia, are typically not a problem in low-inertia ($Re < 1$) microfluidic applications.

Microchannels that are filled with packings, either randomly distributed by packing the channel with particles or in a regular fashion by fabricating posts inside the channels, show profoundly different behavior as compared with the multiphase flows that we discussed previously. Figure 1.7 compares different configurations.

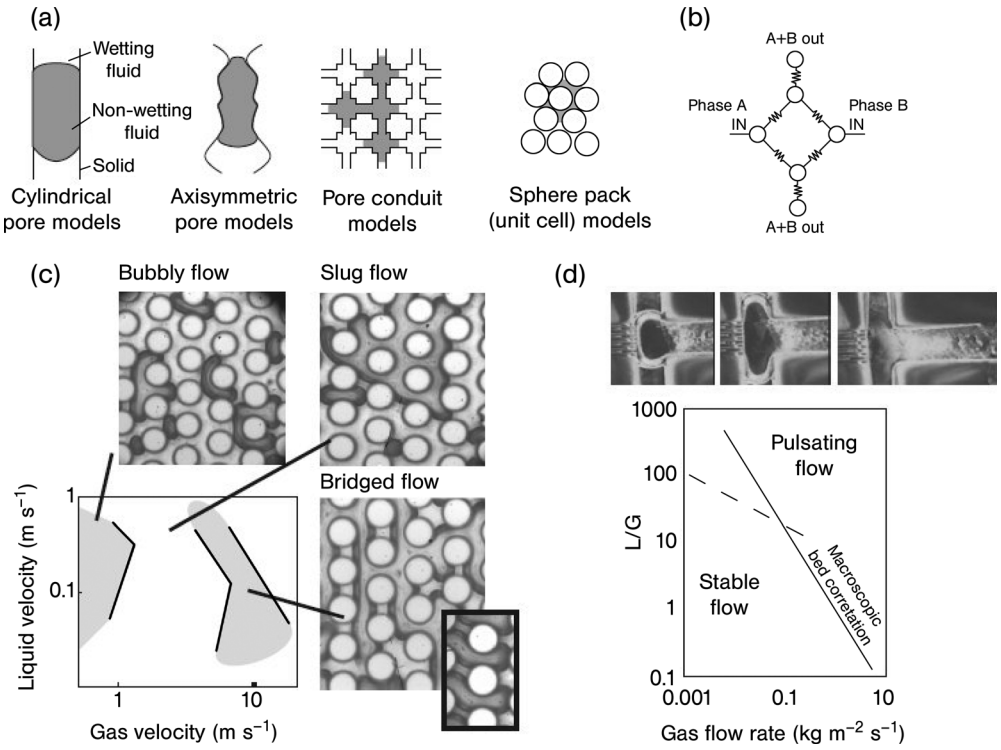

Figure 1.7 Packed-bed microchannels. (a) Two-phase flow in porous media is described using multiscale approaches that seek to combine channel-level descriptions with the analysis of connected networks [108–110]. (b) The description of microfluidic multiphase networks can be modeled with networks-of-resistances models, which require very accurate estimates of the two-phase pressure drop [111]. (c) Two-dimensionally defined channels with posts allow visualization of fluid flow and the construction of flow maps [112]. (d) The flow maps are very dependent on the inlet conditions. Here, the micrographs show the formation of large bubbles that shoot into the channel [25].

A number of these references have yet to be introduced to the reaction engineering community. For example, the range of conditions of current three-phase reactor literature does not cover microfluidic flows. The study of flow in porous media, relevant in oil recovery, is often more appropriate.

1.5 Experimental and Numerical Techniques

This section describes numerical and experimental means for the detailed characterization of multiphase flows. Flow behavior is closely linked to the transport processes of fluid mixing and axial dispersion and therefore affects the yield of chemical reactions performed in microchannel networks. Integrated multiphase flow sensors are potentially important for observing and controlling microreactor performance during continuous operation.

1.5.1 Numerical

Surface tension-dominated flow are challenging numerically because of the Laplace boundary condition at the interface. This makes the shape of the interface part of the solution. One can use a flexible mesh that deforms to satisfy the boundary conditions [99, 113–116]. Such simulations can also be performed using commercially available codes [54, 117] and give good agreement with theory. The drawback of flexible mesh methods is that they are less suited for problems that involve droplet or bubble breakup or merger. An alternative to a flexible mesh is to use a rigid grid and to track the interface movement, using so-called front-tracking codes [118, 119]. Phase-field methods [120, 121] use a phase order parameter to indicate the location of interfaces and are particularly well suited to study breakup and coalescence phenomena using a finite thickness of the interface. Fan and co-workers [122] used lattice–Boltzmann (LB) methods, a kinetic gas theory-based approach, to simulate a flow-focusing device and found good agreement with experiments. Volume-of-fluid (VOF) methods, finite-volume methods that keep track of the volumetric fraction of each phase, are often used in commercial codes such as Fluent, e.g. Qian and Lawal modeled segmented flow in a microchannel [123].

1.5.2 Experimental

The dynamic nature of multiphase microflows imposes unique requirements on the time resolution of the flow characterization techniques. Table 1.1 summarizes different experimental techniques for characterizing microscale multiphase flow and also the spatial and temporal measurement resolutions. Intrusive measurement probes are generally not an option for micro- and nanofluidic systems.

Table 1.1 Experimental techniques available to study multiphase flow in microsystems with their spatial and temporal resolution [50].

Technique	Spatial dimension	Spatial resolution	Temporal resolution
Brightfield microscopy [63]	2D	~1 μm	0.2–33 ms, 18 ns (stroboscopic white light source)
Fluorescence microscopy	2D	~1 μm	33 ms, 7 ns (pulsed Nd:YAG/YLF laser)
Confocal microscopy	2D/3D[a]	~1 μm	~500 ms (2D), ~1 min (3D), ~70 ms (2D),
	2D/3D[b]	~1 μm	0.1–1 min (3D)
Transient magnetic resonance imaging (MRI) [128]	2D/3D	800 μm	150 ms
X-ray tomographic microscopy (XTM) [129–131]	2D/3D	1.1–4 μm	30–90 min (3D)
	2D/3D	<100 nm	
Total internal reflectance sensing [18, 69]	1D	~200 μm	0.1–1 ms
IR and conductivity sensing [132]	1D	Distance between probes 10 mm	0.1 ms

[a] Scanning confocal microscope.
[b] Spinning disk confocal microscope.

1.5.2.1 Brightfield Microscopy

The most often used imaging technique requires direct optical access to the microfluidic network. A popular option is to use bright field microscopy and a sufficiently short camera shutter time. At high flow velocities of ~0.1 cm s^{-1}, relevant to rapid gas–liquid reactions (direct fluorination [17, 18], oxidation reactions) and for studying reaction kinetics in segmented flows at millisecond time scales [124], obtaining sharp images at a spatial resolution of ~1 μm therefore requires a shutter time of 0.1 ms. Digital cameras that acquire several thousand frames per second are often used to record fast transient events such as microdroplet formation and breakup [63, 124]. For camera shutter times below 10 ms, image quality can generally be improved if the continuous light source of a microscope (typical power 100 W) is replaced by a stroboscopic source (Figure 1.8a).

1.5.2.2 Fluorescence Microscopy

If at least one of the liquid phases is fluorescently labeled with an organic dye or with semiconductor nanocrystals (e.g. CdSe quantum dots [125]), fluorescent microscopy reveals the phase distribution, the shape of the fluid interphase or the local species

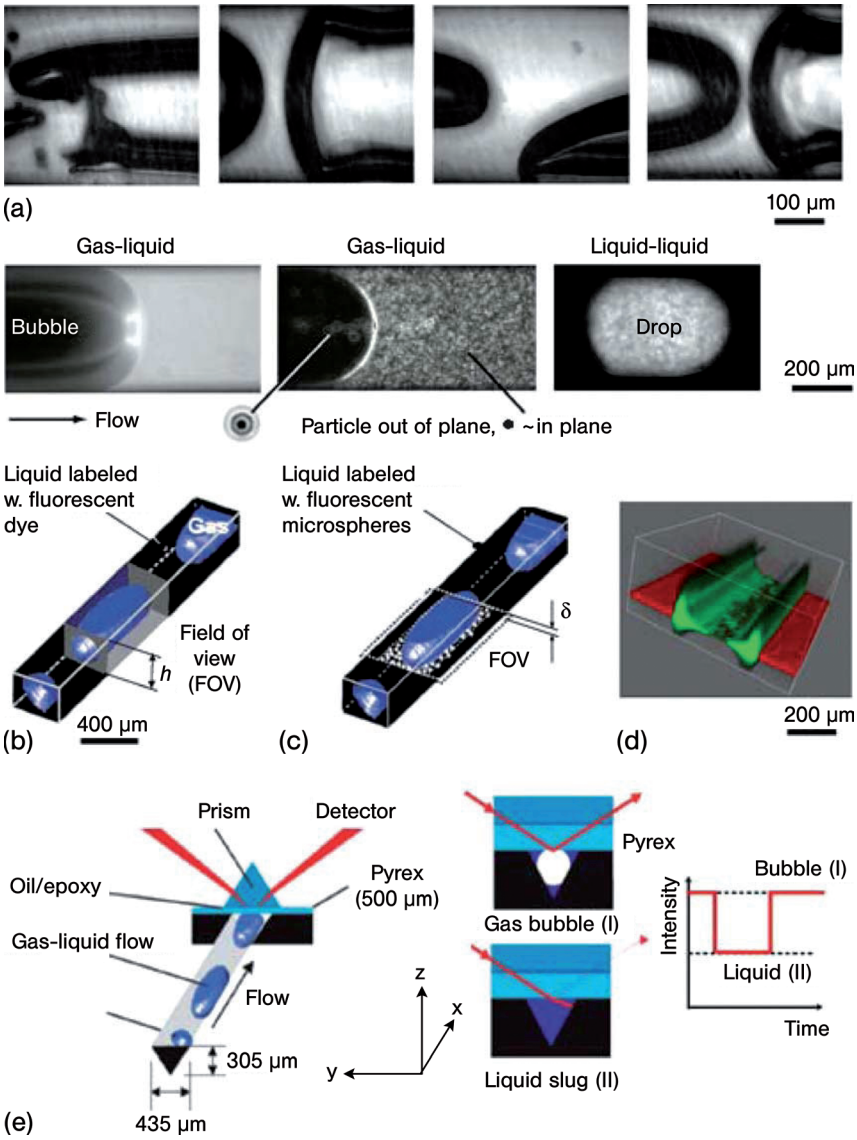

Figure 1.8 Experimental techniques for characterization of microscale multiphase flows. (a) Time series of images from brightfield microscopy using a 25 mJ flash (100 ns) as a white light source. Gas–liquid flows at high superficial velocities in the slug and churn regimes are visualized in a 400 mm wide microchannel. (b) Fluorescent whole-field microscopy using a continuous light source or pulsed (7 ns) laser light. One phase of a segmented microflow is fluorescently labeled. (c) Pulse-laser microscopy with fluorescent microspheres. Cross-correlating two subsequent fluorescent micrographs allows to obtain velocity vector fields (µPIV). (d) 3D reconstruction of the phase distribution as obtained from scanning confocal measurements in annular gas–liquid flow through a rectangular channel of width 400 mm and depth 380 mm. (quantum-dot seeded ethanol stream, green; Pyrex wall, red). Note that the partially de-wetted liquid film is well resolved. (e) Total internal reflection (TIR)-based, scalable flow regime sensor [69].

concentration inside one phase in a multiphase microfluidic network (Figure 1.8b). However, for time-dependent microflows (e.g. bubble and droplet flows), the light intensity required for fluorescent images to be sharp is often too small to use continuous light. At bubble/droplet velocities of $0.1\,m\,s^{-1}$, an exposure time of less than 100 ns is required to reduce image distortions below 10 μm. Pulsed solid-state lasers (Nd:YAG, Nd:YLF) with very short pulse durations (~10 ns) are useful for this task and synchronized to intensified CCD or CMOS cameras. The entire microchannel depth is illuminated and the collected fluorescence information is integrated over the entire channel depth, h (Figure 1.8b).

1.5.2.3 Particle Tracking and Particle Image Velocimetry

Seeding at least one liquid phase with fluorescently labeled microparticles (Figure 1.8c) allows an image plane within the liquid phase to be selected with a depth of focus δ that corresponds to the magnification, M, and numerical aperture, NA, of the microscope objective. Particles located within δ produce sharp images whereas those located outside appear blurred and at reduced intensity. Inoue and Spring [126] estimated the total depth of field as a sum of the depth of field due to diffraction and geometric effects:

$$\delta = \frac{n\lambda}{NA^2} + \frac{ne}{M \cdot NA} \tag{1.5}$$

where n is the refractive index of the immersion medium between the microfluidic device and the objective lens, λ is the wavelength of light in a vacuum, NA is the numerical aperture of the objective lens, M is the total magnification of the system and e is the smallest resolvable distance at the image detector [126, 127].

Typical values for δ in microscale particle image velocimetry (μPIV) measurements are between 0.5 and 5 μm. The technique determines velocity vector fields within the depth of field by locally cross-correlating two successive particle images and thereby determining the local displacement of the seeding particle images [127, 133]. Applying μPIV to the disperse phase in multiphase systems is generally a challenge due to the different refractive indices and refraction of light at curved fluid interfaces. Effects that are particularly pronounced for microscale gas–liquid flows (water–air has a refractive index ratio of 1.333 compared with 1.01 for water–perfluorodecalin). The dominance of surface tension and the regularity of interfaces (microbubbles/drops) in microscale flows are advantages and make PIV a much more suitable technique to study microscale multiphase flows than in the macroscale case.

Observations are unaffected by refraction at the fluid interface for measurements in the continuous fluid phase, but they are affected if the velocity is determined in the discrete phase (velocity field inside microdrops). Image resolution close to the microchannel walls and in the proximity of the fluid interface is limited by reflections and aperture effects, regions that should be masked before performing the cross-correlation. Several μPIV results have been obtained in segmented gas–liquid flows [50, 80, 86]. For steady or periodic flows, two-dimensional velocity

fields can be reconstructed by successively obtaining velocity fields in different image planes.

1.5.2.4 Confocal Microscopy

The technique excludes out-of-plane information in fluorescence measurements and allows, for steady systems, three-dimensional information to be acquired slice-by-slice. It is therefore often the technique of choice to obtain local intensity measurements for steady microscale flow and transport problems. However, for multiphase microfluidic systems, poor temporal 3D resolution often limits the applicability of the technique. The confocal technique is available in scanning confocal microscopes, in which one confocal laser beam scans the image plane line-by-line and the intensity is collected in a photomultiplier tube and in spinning (Nipkow) disk microscopes [134], in which an array of confocal beams scans the image plane. Imaging one image plane with the spinning disk technique is often limited to a single color and typically takes <70 ms. Scanning confocal microscopes can simultaneously scan multiple wavelengths, but their time resolution of $\sim$1 s per plane is relatively slow. For time-dependent measurements, e.g. to study transport processes in segmented flows, the first technique is often preferred. At low flow rates of liquid-suspended fluorescent particles, the time resolution of the spinning disk technique is even sufficient to cross-correlate subsequent image frames and perform PIV [135].

1.5.2.5 Flow Sensors

Microscopy often implies an expensive means to characterize flows, in particular for (routinely) observing flow regimes highly parallel (scaled-out) multiphase microfluidic networks. Therefore, there is interest in the availability of scalable and non-intrusive sensor concepts that can be integrated in a variety of microfluidic devices without major design modifications, provide basic flow characterization and serve as monitoring tools, e.g. to determine whether channels are plugged or distinguish between segmented an annular regimes. Wolffenbuttel *et al.* [132] combined IR absorption with a capacitance sensor to analyze gas–liquid–solid flows and Kraus *et al.* [69] used total internal reflection (TIR) of laser light at a fluid interface to characterize flow regimes at up to 10 kHz (Figure 1.8e). The latter measurement system was then integrated in a multilayer, multichannel device to demonstrate its scalability and application in situations where direct optical access to the flow channel was not available [18].

1.5.2.6 Magnetic Resonance Imaging

Tomographic techniques are powerful but expensive tools to obtain flow regime information in microfluidic networks, particularly where direct optical access is not available, e.g. in multilayer stacked microreactors or inside microstructured reaction channels. Magnetic resonance imaging (MRI) is currently used for characterizing single- and multiphase flows inside parallel flow channels of monolith reactors. The single excitation multiple image rapid acquisition with relaxation enhancement (SEMI-RARE) technique reported by Gladden's group [128, 136] provides a temporal resolution of 156 ms and a spatial resolution of $371 \times 782\,\mu$m (at an image slice

thickness of 800 μm). Although the spatial and temporal resolution of current MRI systems is limited, the technique is very promising for basic flow regime studies in scaled-out microreactor units.

1.5.2.7 **X-ray Tomography**

High spatial resolution phase distribution measurements in microchannels can be achieved with X-ray projection imaging or by X-ray tomographic microscopy (XTM) using synchrotron radiation. XTM capabilities are installed at several beamline facilities and provide a spatial resolution of ca. 4 μm for a 10 mm^3 measuring volume [129, 130]. The temporal resolution can vary significantly anywhere from several seconds (in the case of projection imaging) up to several hours (for tomographic reconstruction), depending on the detail of reconstruction, the tolerated noise level and the absorption in wall surfaces. Synchrotron XTM is a powerful technique that is often used to characterize microstructured materials, e.g. the microstructure of bone, the microvascular network [137], condensed soft matter and biological cells [131], and has previously been applied to multiphase flow studies in porous materials [138]. State-of-the-art systems for cellular applications can achieve a spatial resolution below 100 nm. A general fabrication challenge for transient synchrotron XTM measurements is to reduce absorption from side-walls, e.g. by confining the multiphase flows studies between ~100 nm thin SiN channel walls.

1.6
Annular and Stratified Two-phase Flows

For annular flows, all microchannel walls are covered with continuous thin layers of liquid, where the core of the channel is filled with either a gas or a second, immiscible liquid. Wetting properties of the microchannel wall are of key importance, particularly at low flow rates. The film is preferentially formed by the wetting fluid [67]. Stable annular flows are formed at high superficial velocities and a flow rate of the film phase that is significantly lower than that of the core phase. At very high flow rates of the core phase, the interface is susceptible to interfacial instabilities and forms waves that disintegrate into more complex phase distributions. At low flow rates, capillary forces vastly dominate over viscous or inertial forces, conditions that favor the formation of segmented flows. Annular flows have found a range of different applications in microreactor research. Non-catalytic gas–liquid reactions, e.g. direct fluorinations, have been performed either under annular flow conditions or close to the transition line to segmented flows [18, 23, 88, 139].

Instabilities of a fluid–fluid interface can be prevented by patterning the internal surface of a microchannel to create hydrophilic and hydrophobic paths [43]. Capillary forces can then be used to create precisely controlled vertical interfaces or "virtual walls" between two immiscible fluids with different wetting behavior [140]. Such pinned interfaces result in large interfacial areas for efficient mass transfer between the two phases and have previously been used for microfluidic extraction in co-flow and cross-flow configurations [93]. Kenis *et al.* have guided miscible liquids in

microfluidic networks and used the technique for selectively patterning sections of the microchannel [141]. The same group created an "air breathing" fuel cell by confining thin sheaths of a liquid between two bounding gas streams [142].

1.7 Droplet and Bubble Flows

The formation of droplets and bubbles in a continuous phase has attracted attention ever since Lord Rayleigh in 1879 studied the breakup of fluid jets [43, 143] and Taylor investigated stability criteria of droplet/bubble formation [144]. The most common flow patterns in microfluidic reactor applications involve discrete bubbles or droplets. Droplets can be generated at moderate to high frequencies in passive microfluidic systems where Rayleigh or Rayleigh–Plateau instabilities (e.g. Figure 1.4a) govern droplet formation, with an upper limit of about 1–10 kHz. Droplets range in size from less than 1 μm for ultrasound contrast agent applications to the large segmented-flow droplets that span the entire cross-section of a microchannel. Active microfluidic systems that rely on an external forcing frequency to induce droplet breakup are often based on acoustic streaming and have demonstrated the production of 24 μm droplets at a rate of 34.7 MHz (Figure 1.4e) [77, 145].

In microreactor applications, the segmented flow pattern (Figure 1.3) is most common. Here, discrete droplets behave as separate reactor vessels that are convected along in the microfluidic network by the continuous carrier liquid. Similarly, the longitudinal dispersion of the continuous phase can be suppressed by the use of discrete droplets or bubbles of the segmenting phase.

1.7.1 Lubrication Analysis

The understanding of segmented flow in capillary channels begins with two now classical papers from the Cavendish Laboratories in Cambridge, published in 1961. In the first paper, Taylor [146] postulated the main features of the possible flow patterns, introducing the recirculating vortex in the slug, separated from the film attached to the wall. In later studies, these features of segmented flow were confirmed using photographs and particle image velocimetry [80, 147–149]. The second paper, by Bretherton [150], used lubrication analysis for the transitional region where the film is formed, i.e. between the spherical front of the bubble and the flat film far behind the front. Lubrication theory was originally developed to explain why no solid-to-solid contact occurs in bearings due to the motion of a lubricating viscous fluid. In segmented flow, the thin film prohibits gas-to-solid contact rather than solid-to-solid contact; the same mathematical treatment of the equations of fluid motion as developed for bearings may be used.

Here only a condensed scaling analysis from Aussilous and Quere [151] is given. The front of the bubble may be regarded as spherical with radius r and the Laplace pressure difference across the gas–liquid interface is given by $\Delta p = 2\gamma/r$, provided

that the film thickness δ is small ($\delta \ll r$). In the region of constant film thickness, the curvature in the axial direction vanishes and here the Laplace pressure difference is given by $\Delta p = \gamma/r$. A balance of the viscous force and the pressure gradient in this transitional region yields

$$\frac{\mu U}{\delta^2} \sim \frac{1}{\lambda}\frac{\gamma}{r} \tag{1.6}$$

where λ is the length of the transitional region between the spherical and flat interface. This length λ is unknown, but we can estimate it by requiring that the Laplace pressure is continuous at the interface or, in other words, that the curvature of the spherical part matches the curvature at the end of the transition region:

$$-\frac{\gamma}{r} - \frac{\gamma\delta}{\lambda^2} \sim -2\frac{\gamma}{r} \tag{1.7}$$

or $\lambda = \sqrt{(\delta r)}$, which yields the now classical scaling rule $\delta/r \sim Ca^{2/3}$. The more rigorous analysis of the full Navier–Stokes equations in the transition region at the front and the back of the bubble by Bretherton yielded the constant of this scaling rule for round channels: $\delta/r = 0.66\, Ca^{2/3}$. At high values of the capillary number, the approximation that $\delta \ll r$ no longer holds [151] and the film thickness has an asymptotic constant value for high *Ca*. This asymptotic value, $\delta \approx 0.4r$, was first reported by Taylor [146].

To estimate the film thickness, an analysis of the front of the bubble suffices. Apart from the film thickness, the matching method also yields the pressure difference between the nose of the bubble and the film. A similar analysis can be made for the rear of the bubble, to give the pressure difference between the film and opposite tip of the bubble. Adding the two pressure differences gives an expression for the pressure drop over the bubble:

$$\frac{\Delta p}{\gamma/r} = 7.16(3Ca)^{2/3} \tag{1.8}$$

The theory of Bretherton agrees nicely with experimental data for low *Ca*. For other geometries, the values of the proportionality constant changes [97–99, 101, 152–154], but the scaling rules remain valid.

The lubrication analysis presented above does not include the effect of inertia, which readily becomes significant for low-viscosity liquids. Inertia has been taken into account in a scaling analysis [151], in numerical studies [54, 114–116, 155] and in experimental pressure drop measurements [54]. Apart from inertia, Marangoni effects, i.e. the gradients of surface tension on the interface due to gradients in temperature or surfactant concentration, can significantly change the film thickness and pressure drop over a bubble. Bretherton estimated the maximum effect of Marangoni convection by repeating the analysis for the front and rear of the bubble, but now with a no-slip boundary condition on the interface instead of a non-shear boundary condition. This did not invalidate the $Ca^{2/3}$ scaling rule, but the numerical values for the pressure drop and film thickness were a factor of $4^{2/3}$ higher than those for a clean, non-rigid interface. The full analysis of these Marangoni effects is much more complex [156–163] and is not discussed here.

1.7.2
Pressure Drop in Segmented-flow Microfluidic Networks

At the small capillary numbers associated by most microfluidic applications, the pressure drop over a bubble is significant with respect to the viscous losses in the continuous liquid. For single-phase laminar flow, velocity and pressure drop are linearly related and the pressure drop is proportional to the length Δz of the channel. For segmented flow, the pressure drop also contains a term that depends on n, the number of segments (i.e. bubbles or droplets) in that channel. For round channels, the two terms are

$$\Delta p_{\mathrm{visc}} = 32\frac{\mu U}{d}\frac{\Delta z}{d}; \quad \Delta p_{\mathrm{seg}} = \frac{14.89}{Ca^{1/3}}\frac{\mu U}{d}n \tag{1.9}$$

These two terms are written as a function of the viscous scale ($\mu U/d$) to facilitate a comparison. For most microfluidic systems, $Ca < 10^{-3}$ or $\mathrm{Ca}^{-1/3} > 10$ and the per-segment pressure drop is $>10^2(\mu U/d)$, which may be compared with the pressure drop in the continuous liquid between the segments of $32(\mu U/d)$ per distance of a channel diameter. One has to be careful when using a linear circuit model ($\Delta p \sim U$) of hydrodynamic resistances [29] for reactor design, because the per-segment term also depends non-linearly on the velocity through the $\mathrm{Ca}^{-1/3}$ factor.

1.8
Practical Aspects of Microfluidic Networks

1.8.1
Parallel Scaling

In this section, we describe how segmented flow properties can be achieved in scalable multiphase microfluidic networks that are independent of internal (flow-related) and external (e.g. pump-related) pressure fluctuations. A desired feature of microchemical systems is the ability to replicate flow, transport and reaction conditions from a single microchannel to many, ideally infinitely many, parallel microchannels. This process is often referred to as *scaling-out*. The concept stands in contrast to scale-up procedures for large-scale equipment in which reactor design and dimensions are increased through a series of time-consuming steps. The following requirements therefore exist to achieve scalable multiphase microsystems:

- equal distribution of multiphase flow properties and prevention of "cross-talk" across a large number of parallel flow channels;
- minimum adverse multiphase flow effects influenced by external or upstream pressure fluctuations (caused either by subsequent multiphase processing steps or by fluctuations in single-phase feed lines);
- prevention of cross-talk between several single-phase and/or multiphase systems that are operated in line.

In Sections 1.2 and 1.7, we have seen that the formation of gas–liquid and liquid–liquid segments is a dynamic phenomenon depending on the flow rates of the two phases (Figure 1.5b and c), the wetting properties of the channel walls and the inflow geometry. Within the segmented flow regime, the time-dependent nature of droplet/bubble breakup causes the flow behavior to be sensitive to external pressure fluctuations. This influence is particularly pronounced at the low flow rates and pressure drops that are typical for segmented gas–liquid flows for liquid-phase reactions. Significantly improved flow regularity was achieved if pressure drop channels were included for all single-phase feed streams [18, 50]. At low flow rates, flow uniformity was achieved if the pressure drop in the single-phase feed lines dominated significantly over the two-phase pressure fluctuations.

Various sources of unstable flow have been discussed in Section 1.3.4. These fluctuations can be reduced if flow restrictions are incorporated in the single-phase feed streams such that the pressure drop across each the feed stream is at least one order of magnitude larger than across the multiphase flow (reaction) channel. Undesired external pressure variations and the time-dependent pressure drop across the multiphase reaction channel are then sufficiently damped and no longer cause significant inequalities in the flow rates through different channels (maldistributions) – an important condition for obtaining robust, scalable multiphase reaction networks. The presence of individual pressure drop channels also avoids undesired communication between neighboring flow channels, which can otherwise lead to gas and liquid periodically switching between adjacent channels [88]. de Mas *et al*. designed and fabricated a 60-channel, three-layer (20 channels per layer) gas–liquid reaction platform as a scalable unit [18]. Integrated flow regime sensors confirmed the replication not only of bulk flow rates for gas and liquid, but also of statistical multiphase flow properties (slug lengths and frequencies) across individual channels and reaction layers. Günther *et al* [50] previously illustrated the realization of the pressure manifold feeding concept in a soft-lithographically patterned microfluidic network that provided very regular segmented flows in the multiphase flow channels at superficial velocities of several millimeters per second that correspond to reaction times on the order of minutes that are required for, e.g., nanoparticle synthesis and for on-chip cell lysis.

In contrast to gas–liquid systems, the preferred flow conditions of segmented liquid–liquid flows generally correspond to significantly higher flow rates (often by at least one order of magnitude), and hence to larger pressure drops. Correspondingly, the two-phase pressure drop is much larger in those systems. In this case, external (e.g. syringe pump-induced) pressure fluctuations can assumed to be independent of flow rate. Pressure fluctuations associated with the formation of segmented flows have also been shown to be independent of *Ca* [64]. In many liquid–liquid systems, pressure fluctuations are therefore small compared with the two-phase pressure drop; and regular segmented flows can often be obtained even without separate pressure-drop channels present. Simultaneous droplet production was demonstrated by Sugiura and co-workers [66, 164] in a silicon-based microfluidic device that contained 150 parallel orifices. Li *et al*. [165] recently used the flow-focusing method in a soft-lithographically patterned four-channel microreactor.

Even though an impressive number of multiphase transport and reaction studies have to date been performed in microfluidic systems, their robust linear and serial integration is only starting to be explored. Present limitations are related to the lack of robust chip-to-chip interconnections and to unit operations (e.g. segmented flow channels, separators and extractors) with fairly narrow sets of flow conditions (throughput, temperatures and pressures). Sahoo *et al.* [166] demonstrated linear integration for multistep chemical synthesis with subsequent reaction and phase separations. Expanding these operational conditions will be an important step towards integrated multiphase microfluidic platforms.

1.8.2 Using Multiphase Flows for Controlling Fluid Paths

Integrated microreaction solutions often require fluid pathways on a chip to be altered between different reaction, separation and detection steps. A variety of active valves for fluid control were previously developed in polymers using soft-lithographic techniques [167–169] and, based on metals and silicon, in the MEMS community. Most of these solutions, however, pose significant challenges with respect either to the chemical and thermal compatibility required for many microchemical systems or to fabrication cost and ease of integration.

Passive means of altering fluid pathways that rely solely on the dominance of interfacial forces in microscale confinements have the potential to offer robust and passive solutions. A number of solutions for capillary-based pumping [170, 171] and flow separation [80, 92, 93] were previously demonstrated. More recently, logic elements such as AND, OR and NOR gates, a toggle flip-flop, a ripple counter, timing restoration and a ring oscillator were realized by bubble motion in microfluidic networks [172, 173] and might offer a passive alternative to active fluid control elements in future designs of integrated microfluidic reaction platforms.

List of Symbols and Abbreviations

d_h	Hydraulic diameter, $= 4A\Gamma^{-1}$ (m)
d_P	Particle size (m)
e	Smallest resolvable distance (m)
g	Gravitational acceleration ($m\,s^{-2}$)
h	Microchannel depth (m)
H	Microchannel height (m)
j_G	Superficial velocity of gas phase ($m\,s^{-1}$)
j_L	Superficial velocity of liquid phase ($m\,s^{-1}$)
L	Length scale (m)
L_B	Bubble length in flow direction (m)
L_d	Droplet length in flow direction (m)
L_S	Slug length in flow direction (m)
M	Magnification

n	Refractive index or number of bubbles/droplets
NA	Numerical aperture
P	Pressure (Pa)
ΔP_{cap}	Capillary pressure difference (Pa)
Q_c	Volumetric flow rate of the continuous fluid phase (m)
Q_d	Volumetric flow rate of the dispersed fluid phase (m)
r	Coordinate in radial direction (m)
R	Tube radius (m)
t	Time scale (s)
U	Velocity ($m\,s^{-1}$)
U_d	Velocity of the dispersed fluid phase ($m\,s^{-1}$)
W	Microchannel width (m)
x	Cartesian (streamwise) coordinate (m)
y	Cartesian coordinate (m)
z	Cartesian coordinate (m)
δ	Film thickness or depth of field (m)
γ	Interfacial tension (N/m)
Γ	Wetted perimeter $= 2(W + H)$ (m)
κ	Interface curvature (m^{-1})
λ	Wavelength of light or length of transitional region at the gas–liquid interface of a bubble inside a microchannel (m)
μ	Absolute viscosity of the continuous fluid phase (Pa s)
μ_d	Absolute viscosity of the dispersed fluid phase (Pa s)
ρ	Fluid density ($kg\,m^{-3}$)
ρ_P	Particle density ($kg\,m^{-3}$)
$\Delta\rho$	Density difference between the two fluid phases ($kg\,m^{-3}$)
σ	Interfacial tension ($N\,m^{-1}$)
θ	Gas–liquid–solid contact angle (°)

Dimensionless Groups

Bo	Bond number $= (\Delta\rho) g d_h^2 \sigma^{-1}$
Ca	Capillary number $= \mu U_d \sigma^{-1}$
Re	Reynolds number $= We/Ca = U_d \rho d_h \mu^{-1}$
We	Weber number $= \rho U_d^2 d_h \sigma^{-1}$

Abbreviations

AJM	Abrasive jet machining, micromachining method
CCD	Charge-coupled device, chip architecture for digital cameras
CMOS	Complementary metal–oxide–semiconductor, chip architecture for digital cameras
DNA	Deoxyribonucleic acid
DRIE	Deep reactive ion etching, high-aspect ratio dry etching method for silicon

EWOD	Electrowetting-on-dielectric
IR	Infrared
KH	Kelvin–Helmholtz flow instability
KOH	Potassium hydroxide etch, silicon wet etching method
LB	Lattice–Boltzmann numerical method
MEMS	Microelectromechanical systems
MRI	Magnetic resonance imaging
PIV	Particle image velocimetry, whole-field velocity measurement technique
PDMS	Polydimethylsiloxane, popular structural material for the fabrication of microfluidic devices based on soft lithography
RTD	Residence time distribution
TIR	Total internal reflection-based measurement technique
VOF	Volume of fluid method, numerical method for the treatment of multiphase systems
XTM	X-ray tomographic microscopy

References

1 W.L. Olbricht, Pore-scale prototypes of multiphase flow in porous media. *Annual Review of Fluid Mechanics*, **1996**, *28*, 187–213.

2 H. Fujioka, J.B. Grotberg, The steady propagation of a surfactant-laden liquid plug in a two-dimensional channel. *Physics of Fluids*, **2005**, *17*, 082102.

3 E. Delamarche, D. Juncker, H. Schmid, Microfluidics for processing surfaces and miniaturizing biological assays. *Advanced Materials*, **2005**, *17*, 2911–2933.

4 J. El-Ali, S. Gaudet, A. Günther, P.K. Sorger, K.F. Jensen, Cell stimulus and lysis in a microfluidic device with segmented gas–liquid flow. *Analytical Chemistry*, **2005**, *77*, 3629–3636.

5 M.T. Kreutzer, F. Kapteijn, J.A. Moulijn, J.J. Heiszwolf, Multiphase monolith reactors: Chemical reaction engineering of segmented flow in microchannels. *Chemical Engineering Science*, **2005**, *60*, 5895–5916.

6 A.A. Darhuber, S.M. Troian, Principles of microfluidic actuation by modulation of surface stresses. *Annual Review of Fluid Mechanics*, **2005**, *37*, 425–455.

7 V. Hessel, P. Angeli, A. Gavriilidis, H. Lowe, Gas–liquid and gas–liquid–solid microstructured reactors: contacting principles and applications. *Industrial and Engineering Chemistry Research*, **2005**, *44*, 9750–9769.

8 K.F. Jensen, Microreaction engineering - is small better? *Chemical Engineering Science*, **2001**, *56*, 293–303.

9 T. Hatakeyama, D.L.L. Chen, R.F. Ismagilov, Microgram-scale testing of reaction conditions in solution using nanoliter plugs in microfluidics with detection by MALDI-MS. *Journal of the American Chemical Society*, **2006**, *128*, 2518–2519.

10 H. Song, J.D. Tice, R.F. Ismagilov, A microfluidic system for controlling reaction networks in time. *Angewandte Chemie International Edition*, **2003**, *42*, 768–772.

11 B. Zheng, R.F. Ismagilov, A microfluidic approach for screening submicroliter volumes against multiple reagents by using preformed arrays of nanoliter plugs in a three-phase liquid/liquid/gas flow. *Angewandte Chemie International Edition*, **2005**, *44*, 2520–2523.

12 R.D. Chambers, M.A. Fox, D. Holling, T. Nakano, T. Okazoe, G. Sandford, Elemental fluorine – Part 16, Versatile thin-film gas–liquid multi-channel microreactors for effective scale-out. *Lab on a Chip*, **2005**, *5*, 191–198.

13 R.D. Chambers, M.A. Fox, G. Sandford, Elemental fluorine – Part 18. Selective direct fluorination of 1,3-ketoesters and 1,3-diketones using gas/liquid microreactor technology. *Lab on a Chip*, **2005**, *5*, 1132–1139.

14 R.D. Chambers, D. Holling, A.J. Rees, G. Sandford, Microreactors for oxidations using fluorine. *Journal of Fluorine Chemistry*, **2003**, *119*, 81–82.

15 R.D. Chambers, D. Holling, R.C.H. Spink, G. Sandford, Elemental fluorine – Part 13. Gas–liquid thin film microreactors for selective direct fluorination. *Lab on a Chip*, **2001**, *1*, 132–137.

16 R.D. Chambers, R.C.H. Spink, Microreactors for elemental fluorine. *Chemical Communications*, **1999**, 883–884.

17 de Mas, N., A. Guenther, M.A. Schmidt, K.F. Jensen, Microfabricated multiphase reactors for the selective direct fluorination of aromatics. *Industrial and Engineering Chemistry Research*, **2003**, *42*, 698–710

18 de Mas, N., A. Gunther, T. Kraus, M.A. Schmidt, K.F. Jensen, Scaled-out multilayer gas–liquid microreactor with integrated velocimetry sensors. *Industrial and Engineering Chemistry Research*, **2005**, *44*, 8997–9013.

19 V. Hessel, P. Lob, H. Lowe, Direct fluorination of aromatics with elemental fluorine in microstructured reactors. *Chimica Oggi – Chemistry Today*, **2004**, *22*, 10.

20 K. Kawai, T. Ebata, T. Kitazume, The synthesis of fluorinated materials in microreactors. *Journal of Fluorine Chemistry*, **2005**, *126*, 956–961.

21 B.P. Mason, K.E. Price, J.L. Steinbacher, A.R. Bogdan, D.T. McQuade, Greener approaches to organic synthesis using microreactor technology. *Chemical Reviews*, **2007**, *107*, 2300–2318.

22 R.S. Besser, X. Ouyang, H. Surangalikar, Hydrocarbon hydrogenation and dehydrogenation reactions in microfabricated catalytic reactors. *Chemical Engineering Science*, **2003**, *58*, 19–26.

23 J. Kobayashi, Y. Mori, K. Okamoto, R. Akiyama, M. Ueno, T. Kitamori, S. Kobayashi, A microfluidic device for conducting gas–liquid–solid hydrogenation reactions. *Science*, **2004**, *304*, 1305–1308.

24 M.W. Losey, R.J. Jackman, S.L. Firebaugh, M.A. Schmidt, K.F. Jensen, Design and fabrication of microfluidic devices for multiphase mixing and reaction. *Journal of Microelectromechanical Systems*, **2002**, *11*, 709–717.

25 M.W. Losey, M.A. Schmidt, K.F. Jensen, Microfabricated multiphase packed-bed reactors: characterization of mass transfer and reactions. *Industrial and Engineering Chemistry Research*, **2001**, *40*, 2555–2562.

26 C.J. Gerdts, D.E. Sharoyan, R.F. Ismagilov, A synthetic reaction network: chemical amplification using nonequilibrium autocatalytic reactions coupled in time. *Journal of the American Chemical Society*, **2004**, *126*, 6327–6331.

27 E.M. Chan, A.P. Alivisatos, R.A. Mathies, High-temperature microfluidic synthesis of CdSe nanocrystals in nanoliter droplets. *Journal of the American Chemical Society*, **2005**, *127*, 13854–13861.

28 S.A. Khan, A. Guenther, M.A. Schmidt, K.F. Jensen, Microfluidic synthesis of colloidal silica. *Langmuir*, **2004**, *20*, 8604–8611.

29 S.A. Khan, K.F. Jensen, Microfluidic synthesis of titania shells on colloidal silica. *Advanced Materials*, **2007**, *19*, 2556.

30 B.K.H. Yen, A. Guenther, M.A. Schmidt, K.F. Jensen, M.G. Bawendi, A microfabricated gas–liquid segmented flow reactor for high-temperature synthesis: the case of CdSe quantum dots.

Angewandte Chemie International Edition, **2005**, *44*, 5447–5451.

31 B.K.H. Yen, N.E. Stott, K.F. Jensen, M.G. Bawendi, A continuous flow microcapillary reactor for the preparation of a size series of CdSe nanocrystals. *Advanced Materials*, **2003**, *15*, 1858–1862.

32 B. Zheng, L.S. Roach, R.F. Ismagilov, Screening of protein crystallization conditions on a microfluidic chip using nanoliter-size droplets. *Journal of the American Chemical Society*, **2003**, *125*, 11170–11171.

33 B. Zheng, J.D. Tice, R.F. Ismagilov, Formation of arrayed droplets of soft lithography and two-phase fluid flow and application in protein crystallization. *Advanced Materials*, **2004**, *16*, 1365–1368.

34 R.E. Thiers, A.H. Reed, K. Delander, Origin of lag phase of continuous-flow analysis curves. *Clinical Chemistry*, **1971**, *17*, 42.

35 M.A. Burns, B.N. Johnson, S.N. Brahmasandra, K. Handique, J.R. Webster, M. Krishnan, T.S. Sammarco, P.M. Man, D. Jones, D. Heldsinger, C.H. Mastrangelo, D.T. Burke, An integrated nanoliter DNA analysis device. *Science*, **1998**, *282*, 484–487.

36 S. Sugiura, T. Oda, Y. Izumida, Y. Aoyagi, M. Satake, A. Ochiai, N. Ohkohchi, M. Nakajima, Size control of calcium alginate beads containing living cells using micro-nozzle array. *Biomaterials*, **2005**, *26*, 3327–3331.

37 V.S. Ajaev, G.M. Homsy, Modeling shapes and dynamics of confinded bubbles. *Annual Review of Fluid Mechanics*, **2006**, *38*, 227–307.

38 D. Bartolo, F. Bouamrirene, E. Verneuil, A. Buguin, P. Silberzan, S. Moulinet, Bouncing or sticky droplets: impalement transitions on superhydrophobic micropatterned surfaces. *Europhysics Letters*, **2006**, *74*, 299–305.

39 A. Lafuma, D. Quere, Superhydrophobic states. *Nature Materials*, **2003**, *2*, 457–460.

40 D. Quere, A. Lafuma, J. Bico, Slippy and sticky microtextured solids. *Nanotechnology*, **2003**, *14*, 1109–1112.

41 A.A. Darhuber, J.M. Davis, S.M. Troian, W.W. Reisner, Thermocapillary actuation of liquid flow on chemically patterned surfaces. *Physics of Fluids*, **2003**, *15*, 1295–1304.

42 J.C.T. Eijkel van den Berg A. Water in micro- and nanofluidics systems described using the water potential *Lab on a Chip*, **2005** *5*, 1202–1209

43 J. Atencia, D.J. Beebe Controlled microfluidic interfaces. *Nature*, **2005**, *437*, 648–655.

44 L. Courbin, E. Denieul, E. Dressaire, M. Roper, A. Ajdari, H.A. Stone, Imbibition by polygonal spreading on microdecorated surfaces. *Nature Materials*, **2007**, *6*, 661–664.

45 S.K. Cho, H.J. Moon, C.J. Kim, Creating, transporting, cutting and merging liquid droplets by electrowetting-based actuation for digital microfluidic circuits. *Journal of Microelectromechanical Systems*, **2003**, *12*, 70–80.

46 M.G. Pollack, A.D. Shenderov, R.B. Fair, Electrowetting-based actuation of droplets for integrated microfluidics. *Lab on a Chip*, **2002**, *2*, 96–101.

47 H.W. Lu, F. Bottausci, J.D. Fowler, A.L. Bertozzi, C. Meinhart, C.J. Kim, A study of EWOD-driven droplets by PIV investigation. *Lab on a Chip*, **2008**, *8*, 456–461.

48 J.C.T. Eijkel, B. Dan, H.W. Reemeijer, D.C. Hermes, J.G. Bomer, A. van den Berg, Strongly accelerated and humidity-independent drying of nanochannels induced by sharp corners. *Physical Review Letters*, **2005**, *95*, 256107.

49 K.P. Nichols, H. Gardeniers, A digital microfluidic system for the investigation of pre-steady-state enzyme kinetics using rapid quenching with MALDI-TOF mass spectrometry. *Analytical Chemistry*, **2007**, *79*, 8699–8704.

50 A. Günther, K.F. Jensen, Multiphase microfluidics: from flow characteristics to

chemical and materials synthesis. *Lab on a Chip*, **2006**, *6*, 1487–1503.

51 E. Ory, H. Yuan, A. Prosperetti, S. Popinet, S. Zaleski, Growth and collapse of a vapor bubble in a narrow tube. *Physics of Fluids*, **2000**, *12*, 1268–1277.

52 T. Ye, J.L. Bull, Direct numerical simulations of micro-bubble expansion in gas embolotherapy. *Journal of Biomechanical Engineering – Transactions of the ASME*, **2004**, *126*, 745–759.

53 Y. Zheng, H. Fujioka, J.B. Grotberg, Effects of gravity, inertia and surfactant on steady plug propagation in a two-dimensional channel *Physics of Fluids* **2007**, *19*, 082107.

54 M.T. Kreutzer, F. Kapteijn, J.A. Moulijn, C.R. Kleijn, J.J. Heiszwolf, Inertial and interfacial effects on pressure drop of Taylor flow in capillaries. *AIChE Journal*, **2005**, *51*, 2428–2440.

55 K. Jahnisch, V. Hessel, H. Lowe, M. Baerns, Chemistry in microstructured reactors. *Angewandte Chemie International Edition*, **2004**, *43*, 406–446.

56 P.G. Drazin, W.H. Reid, *Hydrodynamic Stability.* Cambridge University Press, Cambridge, **1981**.

57 S. Chandrasekhar, *Hydrodynamic and Hydromagnetic Stability.* Oxford University Press, Oxford, **1968**.

58 J.M. Rallison, The deformation of small viscous drops and bubbles in shear flows. *Annual Review of Fluid Mechanics*, **1984**, *16*, 45–66.

59 H.A. Stone, Dynamics of drop deformation and breakup in viscous fluids. *Annual Review of Fluid Mechanics*, **1994**, *26*, 65–102.

60 A.M. Ganan-Calvo, Generation of steady liquid microthreads and micron-sized monodisperse sprays in gas streams. *Physical Review Letters*, **1998**, *80*, 285–288.

61 A.M. Ganan-Calvo, J.M. Gordillo, Perfectly monodisperse microbubbling by capillary flow focusing. *Physical Review Letters*, **2001**, *87*, 274501.

62 S.L. Anna, N. Bontoux, H.A. Stone, Formation of dispersions using "flow focusing" in microchannels. *Applied Physics Letters*, **2003**, *82*, 364–366.

63 D.R. Link, S.L. Anna, D.A. Weitz, H.A. Stone, Geometrically mediated breakup of drops in microfluidic devices. *Physical Review Letters*, **2004**, *92*, 054503.

64 P. Garstecki, M.J. Fuerstman, H.A. Stone, G.M. Whitesides, Formation of droplets and bubbles in a microfluidic T-junction – scaling and mechanism of breakup. *Lab on a Chip*, **2006**, *6*, 437–446.

65 P. Garstecki, M.J. Fuerstman, G.M. Whitesides, Nonlinear dynamics of a flow-focusing bubble generator: an inverted dripping faucet. *Physical Review Letters*, **2005**, *94*, 234502.

66 S. Sugiura, M. Nakajima, M. Seki, Effect of channel structure on microchannel emulsification. *Langmuir*, **2002**, *18*, 5708–5712.

67 T. Cubaud, C.M. Ho, Transport of bubbles in square microchannels. *Physics of Fluids*, **2004**, *16*, 4575–4585.

68 P. Garstecki, I. Gitlin, W. DiLuzio, G.M. Whitesides, E. Kumacheva, H.A. Stone, Formation of monodisperse bubbles in a microfluidic flow-focusing device. *Applied Physics Letters*, **2004**, *85*, 2649–2651.

69 T. Kraus, A. Günther, N. de Mas, M.A. Schmidt, K.F. Jensen, An integrated multiphase flow sensor for microchannels. *Experiments in Fluids*, **2004**, 819–832.

70 P. Garstecki, M.J. Fuerstman, G.M. Whitesides, Oscillations with uniquely long periods in a microfluidic bubble generator. *Nature Physics*, **2005**, *1*, 168–171.

71 L.Y. Chu, A.S. Utada, R.K. Shah, J.W. Kim, D.A. Weitz, Controllable monodisperse multiple emulsions. *Angewandte Chemie International Edition*, **2007**, *46*, 8970–8974.

72 T. Thorsen, S.J. Maerkl, S.R. Quake, Microfluidic large-scale integration. *Science*, **2002**, *298*, 580–584.

73 J. Kameoka, R. Orth, B. Ilic, D. Czaplewski, T. Wachs, H.G. Craighead, An electrospray ionization source for

integration with microfluidics. *Analytical Chemistry*, **2002**, *74*, 5897–5901.

74 H. Kim, D.W. Luo, D. Link, D.A. Weitz, M. Marquez, Z.D. Cheng, Controlled production of emulsion drops using an electric field in a flow-focusing microfluidic device. *Applied Physics Letters*, **2007**, *91*, 133106.

75 T. Cubaud, T.G. Mason, Folding of viscous threads in diverging microchannels. *Physical Review Letters*, **2006**, *96*, 114501.

76 T. Cubaud, T.G. Mason, Swirling of viscous fluid threads in microchannels. *Physical Review Letters*, **2007**, *98*. 264501.

77 U. Demirci, Acoustic picoliter droplets for emerging applications in semiconductor industry and biotechnology. *Journal of Microelectromechanical Systems*, **2006**, *15*, 957–966.

78 T. Funada, D.D. Joseph, Viscous potential flow analysis of Kelvin–Helmholtz instability in a channel. *Journal of Fluid Mechanics*, **2001**, *445*, 263–283.

79 A. Serizawa, Z.P. Feng, Z. Kawara, Two-phase flow in microchannels. *Experimental Thermal and Fluid Science*, **2002**, *26*, 703–714.

80 A. Günther, S.A. Khan, M. Thalmann, F. Trachsel, M.A. Schmidt, K.F. Jensen, Transport and reaction in microscale segmented gas–liquid flow. *Lab on a Chip*, **2004**, *4*, 278–246.

81 R. Dreyfus, P. Tabeling, H. Willaime, Ordered and disordered patterns in two-phase flows in microchannels. *Physical Review Letters*, **2003**, *90*, 144505.

82 L. Galbiati, P. Andreini, Flow pattern transition for vertical downward 2-phase flow in capillary tubes – inlet mixing effects. *International Communications in Heat and Mass Transfer*, **1992**, *19*, 791–799.

83 K.S. Rezkallah, Weber number based flow-pattern maps for liquid-gas flows at microgravity. *International Journal of Multiphase Flow*, **1996**, *22*, 1265–1270.

84 L. Zhao, K.S. Rezkallah, Gas–liquid flow patterns at microgravity conditions. *International Journal of Multiphase Flow*, **1993**, *19*, 751–763.

85 M. Suo, Pressure drop in capillary slug flow. *Journal of Basic Engineering*, **1968**, *90*, 140.

86 van Steijn, V., M.T. Kreutzer, C.R. Kleijn, mu-PIV study of the formation of segmented flow in microfluidic T-junctions. *Chemical Engineering Science*, **2007**, *62*, 7505–7514.

87 van Steijn, V., M.T. Kreutzer, C.R. Kleijn, Velocity fluctuations of segmented flow in microchannels. *Chemical Engineering Journal*, **2008**, *135*, S159–S165.

88 de Mas, N., A. Günther, M.A. Schmidt, K.F. Jensen, Microfabricated multiphase reactors for the selective direct fluorination of aromatics. *Industrial and Engineering Chemistry Research*, **2003**, *42*, 698–710.

89 P. Burriel, J. Claret, J. Ignes-Mullol, F. Sagues, "Bottleneck effect" in two-dimensional microfluidics. *Physical Review Letters*, **2008**, *100*, 134503.

90 P. Tabeling, *Introduction to Microfluidics*. Oxford University Press, New York, **2005**.

91 N. Reinecke, D. Mewes, Oscillatory transient two-phase flows in single channels with reference to monolithic catalyst supports. *International Journal of Multiphase Flow*, **1999**, *25*, 1373–1393.

92 A. Günther, M. Jhunjhunwala, M. Thalmann, M.A. Schmidt, K.F. Jensen, Micromixing of miscible liquids in segmented gas–liquid flow. *Langmuir*, **2005**, *21*, 1547–1555.

93 A. Hibara, S. Iwayama, S. Matsuoka, M. Ueno, Y. Kikutani, M. Tokeshi, T. Kitamori, Surface modification method of microchannels for gas–liquid two-phase flow in microchips. *Analytical Chemistry*, **2005**, *77*, 943–947.

94 J.G. Kralj, H.R. Sahoo, K.F. Jensen, Integrated continuous microfluidic liquid–liquid extraction. *Lab on a Chip*, **2007**, *7*, 256–263.

95 E. Belloy, A. Sayah, M.A.M. Gijs, Micromachining of glass inertial sensors. *Journal of Microelectromechanical Systems*, **2002**, *11*, 85–90.

96 A. Ghobeity, J.K. Spelt, M. Papini, Abrasive jet micro-machining of planar areas and transitional slopes. *Journal of Micromechanics and Microengineering*, **2008**, *18*, 055014.

97 H. Wong, C.J. Radke, S. Morris, The motion of long bubbles in polygonal capillaries.1, Thin-films. *Journal of Fluid Mechanics*, **1995**, *292*, 71–94.

98 H. Wong, C.J. Radke, S. Morris, The motion of long bubbles in polygonal capillaries.2, Drag, fluid pressure and fluid-flow. *Journal of Fluid Mechanics*, **1995**, *292*, 95–110.

99 A.L. Hazel, M. Heil, The steady propagation of a semi-infinite bubble into a tube of elliptical or rectangular cross-section. *Journal of Fluid Mechanics*, **2002**, *470*, 91–114.

100 A.L. Hazel, M. Heil, Steady finite-Reynolds-number flows in three-dimensional collapsible tubes. *Journal of Fluid Mechanics*, **2003**, *486*, 79–103.

101 W.B. Kolb, R.L. Cerro, Coating the inside of a capillary of square cross-section. *Chemical Engineering Science*, **1991**, *46*, 2181–2195.

102 W.B. Kolb, R.L. Cerro, Film flow in the space between a circular bubbles and a square tube. *Journal of Colloid and Interface Science*, **1993**, *159*, 302–311.

103 W.B. Kolb, R.L. Cerro, The motion of long bubbles in tubes of square cross-section. . *Physics of Fluids A*, **1993**, *5*, 1549–1557.

104 M.T. Kreutzer, A. Günther, K.F. Jensen, Sample dispersion for segmented flow in microchannels with rectangular cross section. *Analytical Chemistry*, **2008**, *80*, 1558–1567.

105 M. Muradoglu, H.A. Stone, Motion of large bubbles in curved channels. *Journal of Fluid Mechanics*, **2007**, *570*, 455–466.

106 A. Günther, S.A. Khan, M. Thalmann, F. Trachsel, K.F. Jensen, Transport and reaction in microscale segmented gas–liquid flow. *Lab on a Chip*, **2004**, *4*, 278–286.

107 M. Muradoglu, H.A. Stone, Mixing in a drop moving through a serpentine channel: a computational study. *Physics of Fluids*, **2005**, *17*, 072109.

108 R.K. Niven, Force stability of pore-scale fluid bridges and ganglia in axisymmetric and non-axisymmetric configurations. *Journal of Petroleum Science and Engineering*, **2006**, *52*, 1–18.

109 P.C. Reeves, M.A. Celia, A functional relationship between capillary pressure, saturation and interfacial area as revealed by a pore-scale network model. *Water Resources Research*, **1996**, *32*, 2345–2358.

110 J. Stark, M. Manga, The motion of long bubbles in a network of tubes. *Transport in Porous Media*, **2000**, *40*, 201–218.

111 F. Jousse, G.P. Lian, R. Janes, J. Melrose, Compact model for multi-phase liquid–liquid flows in micro-fluidic devices. *Lab on a Chip*, **2005**, *5*, 646–656.

112 S. Krishnamurthy, Y. Peles, Gas–liquid two-phase flow across a bank of micropillars. *Physics of Fluids*, **2007**, *19*, 043302.

113 M.D. Giavedoni, F.A. Saita, A free surface flow with compositional-dependent interfacial properties. *Physics of Fluids*, **1996**, *8*, 1371–1383.

114 M.D. Giavedoni, F.A. Saita, The axisymmetric and plane cases of a gas phase steadily displacing a Newtonian liquid – a simultaneous solution of the governing equations. *Physics of Fluids*, **1997**, *9*, 2420–2428.

115 M.D. Giavedoni, F.A. Saita, The rear meniscus of a long bubble steadily displacing a Newtonian liquid in a capillary tube. *Physics of Fluids*, **1999**, *11*, 786–794.

116 M. Heil, Finite Reynolds number effects in the Bretherton problem. *Physics of Fluids*, **2001**, *13*, 2517–2521.

117 R.K. Edvinsson, S. Irandoust, Finite-element analysis of Taylor flow. *AIChE Journal*, **1996**, *42*, 1815–1823.

118 M. Muradoglu, A.D. Kayaalp, An auxiliary grid method for computations of multiphase flows in complex geometries. *Journal of Computational Physics*, **2006**, *26*, 858–877.

119 de Sousa, F.S., N. Mangiavacchi, L.G. Nonato, A. Castelo, M.F. Tome, V.G.

Ferreira, J.A. Cuminato, S. McKee, A front-tracking/front-capturing method for the simulation of 3D multi-fluid flows with free surfaces. *Journal of Computational Physics*, **2004**, *198*, 469–499.

120 De Menech, M., Modeling of droplet breakup in a microfluidic T-shaped junction with a phase-field model. *Physical Review E*, **2006**, *73*, 9.

121 De Menech, M., P. Garstecki, F. Jousse, H.A. Stone, Transition from squeezing to dripping in a microfluidic T-shaped junction. *Journal of Fluid Mechanics*, **2008**, *595*, 141–161.

122 Z. Yu, O. Heraminger, L.S. Fan, Experiment and lattice Boltzmann simulation of two-phase gas–liquid flows in microchannels. *Chemical Engineering Science*, **2007**, *62*, 7172–7183.

123 D.Y. Qian, A. Lawal, Numerical study on gas and liquid slugs for Taylor flow in a T-junction microchannel. *Chemical Engineering Science*, **2006**, *61*, 7609–7625.

124 H. Song, R.F. Ismagilov, Millisecond kinetics on a microfluidic chip using nanoliters of reagents. *Journal of the American Chemical Society*, **2003**, *125*, 14613–14619.

125 C.B. Murray, C.R. Kagan, M.G. Bawendi, Synthesis and characterization of monodisperse nanocrystals and close-packed nanocrystal assemblies. *Annual Review of Materials Science*, **2000**, *30*, 545–610.

126 S. Inoue, K. Spring, *Video Microscopy*. Academic Press, New York, **1997**.

127 C.D. Meinhart, S.T. Wereley, J.G. Santiago, PIV measurements of a microchannel flow. *Experiments in Fluids*, **1999**, *27*, 414–419.

128 J.J. Heras, A.J. Sederman, L.F. Gladden, Ultrafast velocity imaging of single- and two-phase flows in a ceramic monolith. *Magnetic Resonance Imaging*, **2005**, *23*, 387–389.

129 S. Waelchli, Two-phase flow characteristics in gas–liquid microreactors. Dissertation, ETH Zurich, No. 16116, **2005**.

130 J.H. Kinney, M.C. Nichols, X-ray tomographic microscopy (XTM) using synchrotron radiation. *Annual Review of Materials Science*, **1992**, *22*, 121–152.

131 Le Gros, M.A., G. McDermott, C.A. Larabell, X-ray tomography of whole cells. *Current Opinion in Structural Biology*, **2005**, *15*, 593–600.

132 B.M.A. Wolffenbuttel, T.A. Nijhuis, A. Stankiewicz, J.A. Moulijn, Novel method for non-intrusive measurement of velocity and slug length in two- and three-phase slug flow in capillaries. *Measurement Science and Technology*, **2002**, *13*, 1540–1544.

133 J.G. Santiago, S.T. Wereley, C.D. Meinhart, D.J. Beebe, R.J. Adrian, A particle image velocimetry system for microfluidics. *Experiments in Fluids*, **1998**, *25*, 316–319.

134 G.Q. Xiao, T.R. Corle, G.S. Kino, Real-time confocal scanning optical microscope. *Applied Physics Letters*, **1988**, *53*, 716–718.

135 R. Lima, S. Wada, K. Tsubota, T. Yamaguchi, Confocal micro-PIV measurements of three-dimensional profiles of cell suspension flow in a square microchannel. *Measurement Science and Technology*, **2006**, *17*, 797–808.

136 A.J. Sederman, M.D. Mantle, L.F. Gladden, Single excitation multiple image RARE (SEMI-RARE), ultra-fast imaging of static and flowing systems. *Journal of Magnetic Resonance*, **2003**, *161*, 15–24.

137 M. Marxen, M.M. Thornton, C.B. Chiarot, G. Klement, J. Koprivnikar, J.G. Sled, R.M. Henkelman, MicroCT scanner performance and considerations for vascular specimen imaging. *Medical Physics*, **2004**, *31*, 305–313.

138 M.E. Coles, R.D. Hazlett, E.L. Muegge, K.W. Jones, B. Andrews, B. Dowd, P. Siddons, A. Peskin, P. Spanne, W. Soll, Developments in synchrotron X-ray microtomography with applications to flow in porous media. *SPE Reservoir Evaluation and Engineering*, **1998**, *1*, 288–296.

139 K. Jaehnisch, M. Baerns, V. Hessel, W. Ehrfeld, V. Haverkamp, H. Lowe, C. Wille, A. Guber, Direct fluorination of toluene using elemental fluorine in gas/liquid microreactors. *Journal of Fluorine Chemistry*, **2000**, *105*, 117–128.

140 B. Zhao, J.S. Moore, D.J. Beebe, Surface-directed liquid flow inside microchannels. *Science*, **2001**, *291*, 1023–1026.

141 P.J.A. Kenis, R.F. Ismagilov, G.M. Whitesides, Microfabrication inside capillaries using multiphase laminar flow patterning. *Science*, **1999**, *285*, 83–85.

142 R.S. Jayashree, L. Gancs, E.R. Choban, A. Primak, D. Natarajan, L.J. Markoski, P.J.A. Kenis, Air-breathing laminar flow-based microfluidic fuel cell. *Journal of the American Chemical Society*, **2005**, *127*, 16758–16759.

143 Lord Rayleigh, On the capillary phenomena of jets. *Proceedings of the Royal Society of London, Series A, Mathematical and Physical Sciences*, **1879**, *29*, 71–97.

144 G.I. Taylor, The formation of emulsions in definable fields of flow. *Proceedings of the Royal Society of London, Series A, Mathematical and Physical Sciences*, **1934**, *146*, 501–523.

145 U. Demirci, G. Montesano, Single cell epitaxy by acoustic picolitre droplets. *Lab on a Chip*, **2007**, *7*, 1139–1145.

146 G.I. Taylor, Deposition of a viscous fluid on the wall of a tube. *Journal of Fluid Mechanics*, **1961**, *10*, 161.

147 B.G. Cox, On driving a viscous fluid out of a tube. *Journal of Fluid Mechanics*, **1962**, *14*, 81–96.

148 B.G. Cox, An experimental investigation of the streamlines in viscous fluid expelled from a tube. *Journal of Fluid Mechanics*, **1964**, *20*, 193–200.

149 T.C. Thulasidas, M.A. Abraham, R.L. Cerro, Flow patterns in liquid slugs during bubble-train flow inside capillaries. *Chemical Engineering Science*, **1997**, *52*, 2947–2962.

150 F. Bretherton, The motion of long bubbles in tubes. *Journal of Fluid Mechanics*, **1961**, *10*, 166–188.

151 P. Aussillous, D. Quere, Quick deposition of a fluid on the wall of a tube. *Physics of Fluids*, **2000**, *12*, 2367–2371.

152 H. Wong, The motion of a long bubble in polygonal capillaries at low capillary numbers. Dissertation, Univertiy of California at Berkeley, **1992**.

153 H. Wong, S. Morris, C.J. Radke, 3-Dimensional menisci in polygonal capillaries. *Journal of Colloid and Interface Science*, **1992**, *148*, 317–336.

154 H. Wong, S. Morris, C.J. Radke, 2-Dimensional menisci in nonaxi-symmetric Capillaries. *Journal of Colloid and Interface Science*, **1992**, *148*, 284–287.

155 H. Fujioka, J.B. Grotberg, Steady propagation of a liquid plug in a two-dimensional channel. *Journal of Biomechanical Engineering – Transactions of the ASME*, **2004**, *126*, 567–577.

156 A. Borhan, C.F. Mao, Effect of surfactants on the motion of drops through circular tubes. *Physics of Fluids A*, **1992**, *4*, 2628–2640.

157 C.W. Park, Influence of soluble surfactants on the motion of a finite bubble in a capillary-tube. *Physics of Fluids A*, **1992**, *4*, 2335–2347.

158 K.J. Stebe, D. Barthesbiesel, Marangoni effects of adsorption-desorption controlled surfactants on the leading end of an infinitely long bubble in a capillary. *Journal of Fluid Mechanics*, **1995**, *286*, 25–48.

159 S.N. Ghadiali, D.P. Gaver, The influence of non-equilibrium surfactant dynamics on the flow of a semi-infinite bubble in a rigid cylindrical capillary tube. *Journal of Fluid Mechanics*, **2003**, *478*, 165–196.

160 R. Krechetnikov, G.M. Homsy, Surfactant effects in the Landau–Levich problem. *Journal of Fluid Mechanics*, **2006**, *559*, 429–450.

161 E. Rame, The stagnation point in Marangoni-thickened Landau–Levich type flows. *Physics of Fluids*, **2007**, *19*, 078102.

162 L.W. Schwartz, H.M. Princen, A.D. Kiss, On the motion of bubbles in capillary tubes. *Journal of Fluid Mechanics*, **1986**, *172*, 259–275.

163 S.L. Waters, J.B. Grotberg, The propagation of a surfactant laden liquid plug in a capillary tube. *Physics of Fluids*, **2002**, *14*, 471–480.

164 S. Sugiura, M. Nakajima, J.H. Tong, H. Nabetani, M. Seki, Preparation of monodispersed solid lipid microspheres using a microchannel emulsification technique. *Journal of Colloid and Interface Science*, **2000**, *227*, 95–103.

165 W. Li, E.W.K. Young, M. Seo, Z. Nie, P. Garstecki, C.A. Simmons, E. Kumacheva, Simultaneous generation of droplets with different dimensions in parallel integrated microfluidic droplet generators. *Soft Matter*, **2008**, *4*, 258–262.

166 H.R. Sahoo, J.G. Kralj, K.F. Jensen, Multistep continuous-flow microchemical synthesis involving multiple reactions and separations. *Angewandte Chemie International Edition*, **2007**, *46*, 5704–5708.

167 M.A. Unger, H.P. Chou, T. Thorsen, A. Scherer, S.R. Quake, Monolithic microfabricated valves and pumps by multilayer soft lithography. *Science*, **2000**, *288*, 113–116.

168 W.H. Grover, A.M. Skelley, C.N. Liu, E.T. Lagally, R.A. Mathies, Monolithic membrane valves and diaphragm pumps for practical large-scale integration into glass microfluidic devices. *Sensors and Actuators B*, **2003**, *89*, 315–323.

169 D.B. Weibel, M. Kruithof, S. Potenta, S.K. Sia, A. Lee, G.M. Whitesides, Torque-actuated valves for microfluidics. *Analytical Chemistry*, **2005**, *77*, 4726–4733.

170 N. Goedecke, J. Eijkel, A. Manz, Evaporation driven pumping for chromatography application. *Lab on a Chip*, **2002**, *2*, 219–223.

171 D. Juncker, H. Schmid, U. Drechsler, H. Wolf, M. Wolf, B. Michel, N. de Rooij, E. Delamarche, Autonomous microfluidic capillary system. *Analytical Chemistry*, **2002**, *74*, 6139–6144.

172 M.J. Fuerstman, P. Garstecki, G.M. Whitesides, Coding/decoding and reversibility of droplet trains in microfluidic networks. *Science*, **2007**, *315*, 828–832.

173 M. Prakash, N. Gershenfeld, Microfluidic bubble logic. *Science*, **2007**, *315*, 832–835.

174 J.P. Brody, P. Yager, R.E. Goldstein, R.H. Austin, *Biophys. J.*, **1996**, *71*, 3430–3441.

175 D.J. Beebe, G.A. Hensing, G.M. Walker, *Annu. Rev. Biomed. Eng.*, **2002**, *4*, 261–286.

176 H.A. Stone, A.D. Stroock, A. Ajdarin, *Annu. Rev. Fluid Mech*, **2004**, *36*, 381–411.

177 T. Pfohl, F. Mugele, R. Seemann, S. Herminghaus, *Chem. Phys. Chem.*, **2003**, *4*, 1291–1298.

178 J. Atencia, D.J. Beebe, *Nature*, **2005**, *437*, 648–655.

179 T.M. Squires, R.S. Quake, *Rev. Mod. Phys.*, **2005**, *77*, 977–1026.

180 N.L. Abbott, J.P. Folkers, G.M. Whitesides, *Science–New Series*, **1992**, *257*, 1380–1382.

181 A. Luque, F.A. Perdigones, J. Esteve, J. Monserat, A.M. Gañán-Calvo, J.M. Quero, *J. Microelectromech. Syst.*, **2007**, *16*, 1201–1208.

182 A.M. Gañán-Calvo, R. González-Prieto, P. Riesco-Chueca, M.A. Herrada, M. Flores-Mosquera, *Nature Physics*, **2007**, *3*, 737–742.